

Insight-HXMT View of the BHC Swift J1727.8-1613 during its outburst in 2023

KAUSHIK CHATTERJEE,¹ SANTANU MONDAL,² CHANDRA B. SINGH,¹ AND MUTSUMI SUGIZAKI³

¹South-Western Institute For Astronomy Research, Yunnan University, University Town, Chenggong, Kunming 650500, China

²Indian Institute of Astrophysics, 2nd Block Koramangala, Bengaluru, Karnataka 560034, India

³National Astronomical Observatories, Chinese Academy of Sciences, 20A Datun Road, Chaoyang District, Beijing 100012, China

Submitted to ApJ

ABSTRACT

The transient Galactic black hole candidate Swift J1727.8-1613 went through an outburst for the very first time that started in August 2023 and lasted for almost 6 months. We study the timing and spectral properties of this source using publicly available archival Insight-HXMT data for the first 10 observation IDs that last from MJD 60181 to 60198 with a total of 92 exposures for all three energy bands. We extracted the quasi-periodic oscillation properties by model fitting the power density spectrum and from those properties we designate that the QPOs are type-C in nature. We also conclude that the origin of the QPOs could be the shock instabilities, formed in the transonic accretion flow around black holes. The spectral analysis was performed using simultaneous data from the three on-board instruments LE, ME, and HE of HXMT in the broad energy band of 2 – 150 keV. To achieve the best fit, we needed a combination of interstellar absorption, power-law, multi-color disk-blackbody continuum, gaussian emission/absorption, and power-law reflection by neutral material. From the spectral properties, we found that the source was in an intermediate state at the start of the analysis period and was making a transition toward the softer states. The shock (the boundary layer of the corona) moved inward in progressive days in accordance with the spectral nature. We found that the source is present in a high-inclination binary system. The hydrogen column density was found with an average value of $0.27^{+0.08}_{-0.17} \times 10^{22} \text{ cm}^{-2}$.

Keywords: X-rays: binaries – stars: black holes – stars: individual (Swift J1727.8-1613) – accretion, accretion disk – shock – radiation

1. INTRODUCTION

Black holes (BHs) are one of the end-products of massive stars. Stellar-mass black holes (SBHs) are one of the three types of presently detected BHs. They reside in binary systems with a companion star and most of their radiation comes out in the form of X-rays. Thus, they are called black hole X-ray binaries or BHXRBs. Depending on the mass of the companion star, they can be mainly of two types: low-mass X-ray binaries (LMXRBs) or high-mass X-ray binaries (HMXRBs). LMXRBs consist of type-A or later type of stars whereas the HMXRBs consist of giant O or B-type

of stars (White et al. 1995; Tetarenko et al. 2016). Matter coming from the companion accumulates at a distance from the BH due to lack of viscosity, known as the pile-up radius (Chakrabarti et al. 2019; Chatterjee et al. 2022). Due to the accumulation of more matter, the temperature will rise. This gradual increment of temperature sets in instability at the pile-up, which therefore increases the viscosity. At some point in time when the accumulated matter will gain enough viscosity to push forward, accretion starts. On the other hand, irradiation of the accumulated matter at the outer boundary by the central object can also trigger mass accretion when the temperature of the accumulated matter crosses a critical limit (King & Ritter 1998; Mondal 2020). Thus, these systems make ideal laboratories for studying the physics of accretion. The BHXRBs mostly stay in a quiet dormant state when their flux stays at a very low detection level. Episodically, the radiation level increases by a very large factor and they become easily detectable. This is known as an outburst (Remillard & McClintock 2006). The X-ray luminosity increases by several orders of magnitude during an outburst when compared

Corresponding author: Kaushik Chatterjee

kaushik@ynu.edu.cn, mails.kc.physics@gmail.com

santanu.mondal@iiap.res.in

chandrasingh@ynu.edu.cn

mutsumi@nao.cas.cn

to a quiescence. Depending on the nature of the outburst, the sources are classified into two types: persistent and transient sources. Most of the BHXRBs are transient type of sources. They stay in the dormant state for most of their lifetimes. The luminosity becomes $\sim 10^{35}$ erg s $^{-1}$ during episodic outbursting phase.

During the onset of an outburst, the flux in the light curve changes noticeably. According to nature, the outbursts are divided into two types (Debnath et al. 2010): fast rise slow decay (FRSD) and slow rise slow decay (SRSD). However, there are also some other classified outburst types, e.g., according to Zhang et al. (2019), outbursts can also be classified into glitch, reflare, multipeak, and mini-outburst. There are generally four designated spectral states during a complete BH outburst (Remillard & McClintock 2006). They are known as hard state (HS), hard intermediate state (HIMS), soft intermediate state (SIMS), and soft state (SS). Generally, when an outburst starts, it starts in the HS. Then it slowly moves toward the SS through the HIMS and SIMS (Belloni et al. 2005, 2011, and references within). After it reaches its SS the rising phase generally comes to an end and the outburst starts its decaying phase. In the decaying phase, it goes in the opposite direction and reaches the HS again. When a BH outburst goes through all these states, it is known as a type-I outburst. When the soft state is absent, it is known as a ‘failed’ or type-II outburst.

The radiation spectrum of a BH generally consists of two main components. One is the soft thermal multi-colour blackbody component, which is due to the blackbody radiation of the seed photons in the standard accretion disk (Shakura & Sunyaev 1973; Novikov & Thorne 1973). The other is the hard power-law component, which extends up to very high energies. The origin of this component is due to the inverse Comptonization of a fraction of seed photons from the disk, which are intercepted by a hot Compton cloud (Sunyaev & Titarchuk 1980, 1985; Haardt & Maraschi 1993; Zdziarski et al. 1993; Titarchuk 1994; Chakrabarti & Titarchuk 1995; Życki et al. 1999). When the outburst is in HS, there is very small contribution from the thermal component and mostly the non-thermal component dominates. In SS, the thermal component becomes dominant while in the intermediate states (HIMS and SIMS), the contribution from the two components stays comparable. Other than these two components, other components could also be present in the radiation spectrum of a BH. In the case of a high soft state (HSS), there could be the presence of bulk motion Comptonization (BMC) which takes place due to the relativistic speed of matter when it reaches a very close distance to the BH (Blandford & Payne 1981a,b; Payne & Blandford 1981; Psaltis & Lamb 1997; Borozdin et al. 1999; Psaltis 2001;). It was been recently suggested by Chatterjee et al. (2023) that BMC was present in the radiation spectrum of the BHC MAXI J0637-430. The reprocessed emission plays an important role in the case of BHXRBs. Fraction of electromagnetic radiation can come back from the optically thin and geometrically thick Compton cloud to the optically thick and geometrically thin accretion disk due to the strong gravitational

bending effect of the BH (Riaz et al. 2021). The illumination of the Comptonized photons from the Compton cloud to the accretion disk is known as returning or reprocessed radiation (George & Fabian 1991; Ross & Fabian 2005; Garcia & Kallman 2010). The reflection spectrum is a very important part of the whole radiation spectrum which helps determine many important properties of the source. The reflection radiation can produce some very specific features in the spectrum. One of which is the iron K_{α} emission line at ~ 6.4 keV. This happens when the returning radiation illuminates the disk and there is the fluorescence of ionized Fe. This line emission has a width of the order of ~ 1 eV (Pozdniakov et al. 1979). However, for rotating black holes there are effects like Doppler shift and gravitational broadening which makes the line broadened and for rapidly rotating black holes this line can have two peaks due to red-shifting and blue-shifting of the component. This line emission is a very important aspect in estimating the spin of the BH. There could also be other features like Fe-K absorption edge and Compton hump. These features arise because of counterplay between two phenomena. Which feature will be prominent will be resulted in depending on which phenomenon is dominant. These are also energy-dependent. The interplay between photoelectric absorption and Compton scattering phenomena (Guilbert & Rees 1988; Lightman & White 1988; Fabian et al. 1989) will decide the spectral feature. At higher energies above 20 keV, the scattering will be dominant resulting in a Compton hump, whereas, in low energies, there will be the dominance of photoelectric absorption and the spectrum drops away (Lightman & White 1988). As these features take place at a closer distance from the compact object (here a BH), we can notice broad and asymmetric reflection profiles in the spectrum due to distortion due to high gravitation. Proper modeling of the composite spectrum using different combinations of models can give good information about the physics that is going on there. In this regard, high signal-to-noise (s/n) data in the broadband range, e.g., Insight-HXMT (Zhang et al. 2020) can be very useful.

Apart from the spectral features and variabilities, there are temporal variabilities also. Time variability, which is proportional to the length scale of the photon-emitting region, is as important as X-ray spectroscopy to understand the physical properties of accretion flow dynamics in the region near to the BH. During an outburst, we notice that there are very small time-scale variabilities in the light curves, especially in the high-energy ones. If we make a Fourier transformation of the light curve, we notice that fast variability is present in the power density spectrum or PDS (van der Klis 1989). In the PDS, which is a variation of $P(\nu)$ with ν , the variability is mainly aperiodic, which is a direct consequence that the accretion flow onto the BH is turbulent itself. The aperiodic variability, which is the result of the combination of the variation of the source flux and the variation in Poisson statistics, contains both broadband noise and narrow features. The broadband noise is spread over a large frequency range, whereas the narrow feature is a power peak in narrow frequency ranges. The narrow peak is known as the quasi-

periodic oscillation (QPO), which is one of the most important properties of a BH. There is a break frequency (ν_b) that also characterizes the PDS (van der Klis 1994). The noise is modelled by the power-law function, whereas the QPOs are modelled by one or multiple Lorentzian profiles. In BHs, we see low-frequency QPOs (LFQPOs) mainly due to their geometrical origin. Depending on some properties like the frequency (ν), Q -value ($= \nu/\delta\nu$, where $\delta\nu$ is the full width at half maximum or FWHM), RMS, etc., LFQPOs are classified into three different types: type A, B, and C (Casella et al. 2005). Although the clear origin of QPOs is still a matter of debate at present, several ideas were put forward as to why these features are being observed. Explanations like Lense-Thirring precession (Stella et al. 1999; Ingram et al. 2009), magneto-acoustic waves (Titarchuk et al. 1998), accretion-ejection instability (Tagger & Pellat 1999), shock oscillation model (Molteni et al. 1996; Chakrabarti et al. 2005, 2008, 2015) were put forward to explain the origin of LFQPOs in stellar-mass BHs. The shock oscillation model can give a simultaneous explanation of both the spectral and temporal properties, which makes it a very generally comprehensive model. High-resolution light curve data becomes very useful to study the temporal variability properties of BH. In this regard, Insight-HXMT is also very useful as well as studying the spectral properties.

Apart from these properties and features of a BH outburst, there are a few other estimations that give a direct correspondence between the spectral and temporal properties. A good correlation is observed between the two using just the light curve properties, e.g., the hardness ratio or HR, hardness intensity diagram or HID (Homan et al. 2001). Some model-fitted approaches are also important in this regard, e.g., accretion rate ratio or ARR, accretion rate ratio intensity diagram or ARRID (Mondal et al. 2014; Jana et al. 2016; Chatterjee et al. 2020). The RMS-intensity diagram or RID (Munoz-Darias et al. 2011), and hardness ratio-intensity diagram or HRD (Belloni et al. 2005) are also very important estimates when it comes to correspondence between spectral and temporal properties. In different spectral states, all of these properties show different values, which are quite general for BH outbursts.

The BHC Swift J1727.8-1613 was discovered very recently on 24 August 2023 or MJD 60180 (Kennea & Swift Team 2023). The source was very bright as MAXI (Matsuoka et al. 2009) detected a flux of 7 *Crab* in the 2 – 20 keV energy range. After that multi-wavelength follow-up observations were carried out by several ground-based and space-borne telescope facilities (Baglio et al. 2023; Miller-Jones et al. 2023; Negoro et al. 2023b; O’Connor et al. 2023; Wang & Bellm 2023; Williams-Baldwin et al. 2023). The source is reported to have a distance of $2.7 \pm 0.3 kpc$ (MataSanchez et al. 2024) and a mass of $10 \pm 2 M_\odot$ (Svoboda et al. 2024). The revelation of the presence of hydrogen and helium emission lines in the optical spectrum lead to its classification as an LMXRB (Castro-Tirado et al. 2023). The X-ray spectrum and other properties point to its nature as a BHXRB (Liu et al. 2023; Sunyaev et al. 2023). This was supported strongly

after the detection of type C QPOs (Palmer & Parsotan 2023; Draghis et al. 2023; Bollemeijer et al. 2023; Mereminskiy et al. 2023) and flat radio spectrum (Miller-Jones et al. 2023; Bright et al. 2023). There is X-ray monitoring of the source with many satellites, e.g., NICER, NuSTAR, Insight-HXMT, IXPE, etc. Using IXPE data on September 7, 2023, Veledina et al. (2023) estimated its polarization with a polarization degree (PD) of $4.1\% \pm 0.2\%$ and PA of $2^\circ.2 \pm 1^\circ.3$. There was a further polarization study of the source by Ingram et al. (2023). The presence of evolving LFQPOs at the high energy band of using *AstroSat* data was reported by Nandi et al. (2024). Using X-ray spectroscopy, there were reports about the spectral nature of the source. At the onset of the outburst, the spectral nature was consistent with a hard state with a photon index of power-law (Γ) $\sim 1.5 - 1.7$ (Liu et al. 2023). Then using the NICER observations, Bollemeijer et al. (2023) reported the softening of the spectrum with a substantial contribution of the soft blackbody component after 25 days of the start of the outburst. The presence of LFQPOs was reported by Draghis et al. (2023). Using NICER data on August 29 2023 (MJD 60185), Debnath et al. (2023) reported the presence of a soft time lag of 0.014 ± 0.001 sec between energy bands of 3 – 10 and 0.5 – 3 keV at QPO frequency. With reflection spectroscopy, they found the inclination to be $\sim 87^\circ$.

Here is how this paper unfolds. In §1, we give an introduction. In §2, we describe the observation, data selection, reduction, and analysis. In §3, we portray the results. In §4, we make the discussion about the possible physical origin of our result. And finally, in §5, we make a summary of our results and draw some conclusions.

2. OBSERVATION, DATA SELECTION, REDUCTION, AND ANALYSIS

This source is being extensively monitored by various X-ray satellites, e.g., NICER, NuSTAR, Insight-HXMT, IXPE, etc. For our analysis, we use China’s first dedicated X-ray satellite Insight-High X-ray Modulation Telescope (HXMT; Zhang et al. 2020). In the subsequent subsections, we discuss the data selection, reduction, and analysis, respectively.

2.1. Data Selection

This source was regularly monitored by the Insight-HXMT satellite. In the [data archive](#), observations are available on-demand. At the time of the work, we found that there was a total of 34 observation IDs were available, although 3 of them were not downloadable. Out of those usable 31 observation IDs, we took the first 10 observation IDs. However, unlike other X-ray satellite data, each observation ID in HXMT has several different exposures. Also, some of the observation IDs continue for almost 2 to 3 days. We found that for these first 10 observation IDs, each of them has a minimum of 7 to a maximum of 18 exposures. We checked the analysis of all the exposures for the first 3 observation IDs and found that no significant change was noticed. Thus we did not fit every exposure for each observation ID. The details about the selected data are given in Table 1.

Table 1. List of Data used

Obs. Id. ^[1]	Start Date ^[2]	End Date ^[2]	Start MJD ^[3]	Stop MJD ^[3]	Exp. (s) ^[4]
(1)	(2)	(3)	(4)	(5)	(6)
P0614338001	2023-08-25	2023-08-27	60181.3410	60183.0597	148495
P0614338002	2023-08-27	2023-08-28	60183.0597	60184.2327	137343
P0614338003	2023-08-29	2023-08-31	60185.3075	60187.1589	159958
P0614338004	2023-08-31	2023-09-02	60187.1588	60189.0765	165684
P0614338005	2023-09-02	2023-09-04	60189.0765	60191.0601	171384
P0614338006	2023-09-04	2023-09-06	60191.0601	60193.4447	206034
P0614338008	2023-09-07	2023-09-08	60194.0350	60195.0926	91378
P0614338009	2023-09-08	2023-09-09	60195.0926	60196.0840	85659
P0614338010	2023-09-09	2023-09-10	60196.0840	60197.0754	85653
P0614338011	2023-09-10	2023-09-11	60197.0753	60198.0667	85650

^[1] Column 1 lists each observation ID.

^[2] In columns 2 and 3, we give the start and end date of each observation ID.

^[3] In columns 4 and 5, we give the start and end MJD of each observation ID.

^[4] Column 6 gives the exposure time of each observation ID.

2.2. Data Reduction

Insight-HXMT, China’s first astronomical X-ray satellite, was launched on 2017 June 15 (Zhang et al. 2014, 2020) to observe and study the properties of black holes, neutron stars (NSs), active galactic nuclei (AGNs), and other astronomical phenomena. The main scientific instrument is an array of 18 NaI/CSI phoswich scintillation detectors, each of which covers an effective area of 286 cm². The satellite has three instruments or payloads: High Energy (HE; Liu et al. 2020), Medium Energy (ME; Chen et al. 2020), and Low Energy (LE; Cao et al. 2020). They have an effective area of 5100, 952, and 384 cm² and cover an energy range of 20 – 250, 5 – 30, and 1 – 15 keV, respectively.

After downloading on-demand level-1 data from the archive, we produced cleaned level-2 data for science analysis. This process of cleaning raw data was done in the following way. We first installed the `HXMTDAS`¹ v2.05. Using this software, we run the `hpipeline` command using proper input and output directories. This pipeline performs several subsequent automatic commands for all three instruments. However, some suitable conditions are needed to be provided. Some conditions were set to get a good time interval, e.g., elevation angle > 10°; geomagnetic cutoff rigidity > 8 GeV; pointing offset angle < 0.04°; > 600 s away from the South Atlantic Anomaly (SAA). All these commands altogether extract and clean the raw data and produce cleaned and analyzable science products. This is discussed in the `HXMT manual`² in full details. The specific commands `hespecgen`, `mespecgen`, and `lespecgen` produce the spectra for HE, ME, and LE instruments. Whereas, the

`helcgen`, `melcgen`, and `lelcgen` commands produce the light curve files for the three instruments. `herspgen`, `merspgen`, and `lerspgen` produce suitable response files. The background subtraction for both the timing and spectral data was performed using the commands `hebkmap`, `mebkmap`, and `lebkmap` for instruments HE, ME, and LE, respectively. For χ^2 fit-statistics in XSPEC, we group the spectrum using the `grppha` task of FTOOLS to a minimum of 30 counts per bin. We also set the time bin size to 0.01 s to produce suitable light curves for generating PDS and looking for QPOs.

Using the cleaned spectra and light curves, we analyze the source properties, which are discussed in detail in the very next subsection.

2.3. Data Analysis

We perform timing and spectral analysis of the very first outburst during 2023 of the BHC Swift J1727.8-1613. We have downloaded the daily average light curve using the `MAXI/GSC`³ public archive. Using light curves from all three modules of the HXMT, i.e., LE, ME, and HE, we have produced 0.01 s time-binned light curves first. Using those light curves, we have produced power density spectrum (PDS) by using the fast Fourier transformation (FFT) in the `powspec` task of the `XRONOS` package in the `HEASoft` software. Each observation’s data was subdivided into several intervals, each of which contains 8192 newbins. First, the PDS for each interval is generated and then they are averaged to make a resultant PDS. The PDS is normalized in a way that their integral will give the rms-squared fractional variability. White noise level is subtracted and a geometrical rebinning of -1.02 is used. For some data, we needed to use

¹ <http://hxmt.org/index.php/usersp/dataan>

² <http://hxmtcn.ihep.ac.cn/SoftDoc/501.jhtml>

³ http://maxi.riken.jp/star_data/J1727-162/J1727-162.html

a geometrical rebinning of -1.05 to have a prominent QPO-like nature in the PDS. Using these steps, we searched for LFQPOs. We fit the QPO shape by the use of a Lorentzian model in `powspec` and extract QPO properties like frequency (ν_{qpo}), full-width at half maximum or FWHM, normalization. For many observations, we have found the presence of single or multiple harmonics. We have also extracted their properties by fitting them with a Lorentzian model. We fitted the light curves of all the exposures of the listed 10 observations. We report them in the result section.

For spectral analysis, we have also used all three modules, i.e., LE, ME, and HE and fitted the broadband data in the 2 – 150 keV energy band. Looking for the best fit, we have found that using the combination of `diskbb`, `power-law`, `gaussian`, and `pexrav` models, the data is best fitted. For some observations, we needed to add a `gabs` model to achieve the best fit. For interstellar absorption, we have used the `tbabs` model. Since we are simultaneously fitting all three modules, we have included a `constant` to normalize the three resultant fittings. The following two are our model combination: i) `constant*tbabs*gabs*(diskbb + power-law + gaussian + pexrav)` (for those for which `gabs` was required), ii) `constant*tbabs*(diskbb + power-law + gaussian + pexrav)` (for those for which `gabs` was not required). The spectral analysis was not done for all the exposures of the listed observations. Like the timing analysis, we did not spectrally analyze all the exposures, given in Table A. The spectrally analyzed exposures are marked with ‘*’ in Table A. The reason behind this is that, for timing analysis, we found variations of timing properties within a single day, whereas, for spectral analysis, the properties do not vary that much within such a short time. We report them in the result section.

We note that light curves for the LE instrument were not produced for some exposure IDs although we run the same pipeline for all three instruments. Thus we only represented those exposures MJDs in Table 3 for which all three light curves were available for analysis for uniformity.

3. RESULTS

Using the timing and spectral analysis, we have studied the accretion flow properties of the very recent 2023 outburst of the BHC Swift J1727.8-1613. We studied the QPO properties of the source during the outburst as well as the spectral nature and radiation properties of the source using Insight-HXMT data. We broadly discuss the results in the two subsections below.

3.1. Temporal Properties

Here, we discuss the evolution of the flux and hardness ratio, and QPO properties during the first 10 observation IDs of the outburst.

3.1.1. Outburst Profile and Hardness Ratio

In Figure 1, we show the variation of the flux during the outburst. The outburst started roughly at around MJD 60180

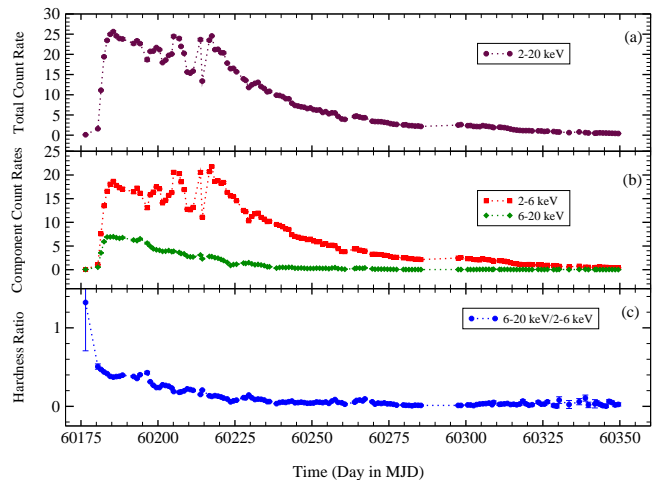


Figure 1. Variation of the (a) MAXI/GSC 2 – 20 keV count rate, (b) MAXI/GSC 2 – 6 and 6 – 20 keV count rates, and (c) hardness ratio with time. The HR is the ratio of the 6 – 20 keV count rate to the 2 – 6 keV count rate of the MAXI/GSC data.

(2023 August 24), when its flux came out of quiescence. The MAXI/GSC flux started to rise after this date, as we can notice from panel (a) of Figure 1. Within five days, the flux increased very rapidly and the total flux reached its peak on MJD 60185 (2023 August 29). Then the flux started to decrease very slowly. It decreased very slowly and gradually except for the period from MJD 60200 to 60225, where the flux showed a significant variation. In panel (b), we show the variations of the 2 – 6 and 6 – 20 keV energy bands count rates with time. We notice that, after MJD 60185, the hard flux (i.e., 6 – 20 keV) decreased very slowly and gradually without showing any other variation, whereas, the soft 2 – 6 keV flux showed a lot of variation just like the total 2 – 20 keV flux. MJD 60185 is the peak for both the total 2 – 20 keV and hard 6 – 20 keV fluxes, whereas, the soft flux reached its peak much later at around MJD 60217. This suggests that the variation in the total count rate is mainly due to the variation of the soft component. After this period, the soft flux also decreased slowly to reach the end of the outburst and enter again into the quiescence phase.

In the panel (c), we show the variation of the hardness ratio, which is the ratio of the hard 6 – 20 keV to the soft 2 – 6 keV flux. At the start of the outburst, the HR was ~ 0.5 . From this value, it first gradually decreased to MJD 60235 as the outburst progressed. After that, it became almost constant, although decreasing very slowly to ~ 0.025 at the end of our taken data of the outburst on MJD 60350. The hardness ratio is defined as F_H/F_S , where F_H and F_S are the hard and soft fluxes respectively. When this value is on the higher side, the spectral nature of the source is hard. This is the general case when an outburst is starting. When this value is low, there is dominance of soft flux over hard flux and the spectral nature would be soft. Without studying the detailed spectral anal-

ysis, HR provides a quick and rough idea about the spectral nature of an outburst. However, for this source, we notice that HR was a little higher at the onset of the outburst, where the hard flux was also comparable to the soft flux. However, after a few days, soft flux completely took over the hard flux, and the HR was also not high. Depending on the HR value, we propose that the source was already in the SIMS after the onset of the outburst. After MJD 60185, it made a transition into the SS. Since we are not analyzing the full duration of the outburst, it is not the scope of the paper to study the full spectral classification. We only spectrally define the source in the duration which falls into our analysis range.

3.1.2. Quasi Periodic Oscillations (QPOs)

As described in §2, we used the 0.01s time-binned light curves from all three bands (LE, ME, and HE) for our timing analysis. Using those light curves, we produced the power density spectrum (PDS) of those light curves to study QPOs. We find that QPO nature was present in all of the light curves in all three energy bands. In Figure 2, we show the variation of the QPO frequency (ν_{qpo}) for the 10 different obs. IDs that we have used for our timing analysis. We first checked the first obs. ID P0614338001. It has several exposure IDs (given in Table 2). While we fit every exposure ID of this obs ID, we found that the QPO frequency was changing even within this small period. This is why we fitted all the light curve data of the exposures of the obs IDs that we have taken for analysis. We find that for every single obs ID, the ν_{qpo} showed significant variation. Figure 2(a), (b), (c) show the variations of the ν_{qpo} with time for 10 different obs IDs for LE, ME, and HE respectively.

In Figure 3, we show the evolution of the ν_{qpo} for the total duration of our analysis period. In (a), (b), and (c) panels the variations are for LE, ME, and HE respectively. We find that the QPO frequencies were $\sim 0.23 \pm 0.008$, 0.24 ± 0.002 , and 0.24 ± 0.002 Hz for LE, ME, and HE on the starting day of our analysis. After this day, the ν_{qpo} shows a rapid increase with time till \sim MJD 60187 when ν_{qpo} was ~ 1.2 Hz for all the three bands. After this date, it increased very slowly till MJD ~ 60190 when ν_{qpo} was ~ 1.45 . Then it decreased for a very short period until it very rapidly increased to 1.5Hz again in all three bands. After that, it showed varying nature till MJD ~ 60197 and then it finally increased again. This might be caused by the varying nature of the origin of these oscillations. We will discuss this in the next section.

Using the PDS fitting, we extracted some information (e.g., full-width at half maximum (FWHM), Normalization (LN)) of QPOs. We also extracted source and background count rates from the exposures. Using these estimates, we calculated the Q -value and RMS that represent the sharpness of the QPO and the fractional variability in the PDS, respectively. The values are listed in Table 3 in columns 5–7 (Q -value) and 8–10 (RMS) for LE, ME, and HE respectively.

In Figure 4, we show a 3-D representation of the evolution of QPO RMS with corresponding frequency. In the LE band (Fig.4a), The RMS was higher at the start of the analysis period and it then gradually decreased. In the ME band

Evolution of QPO frequency in different observation ID.s

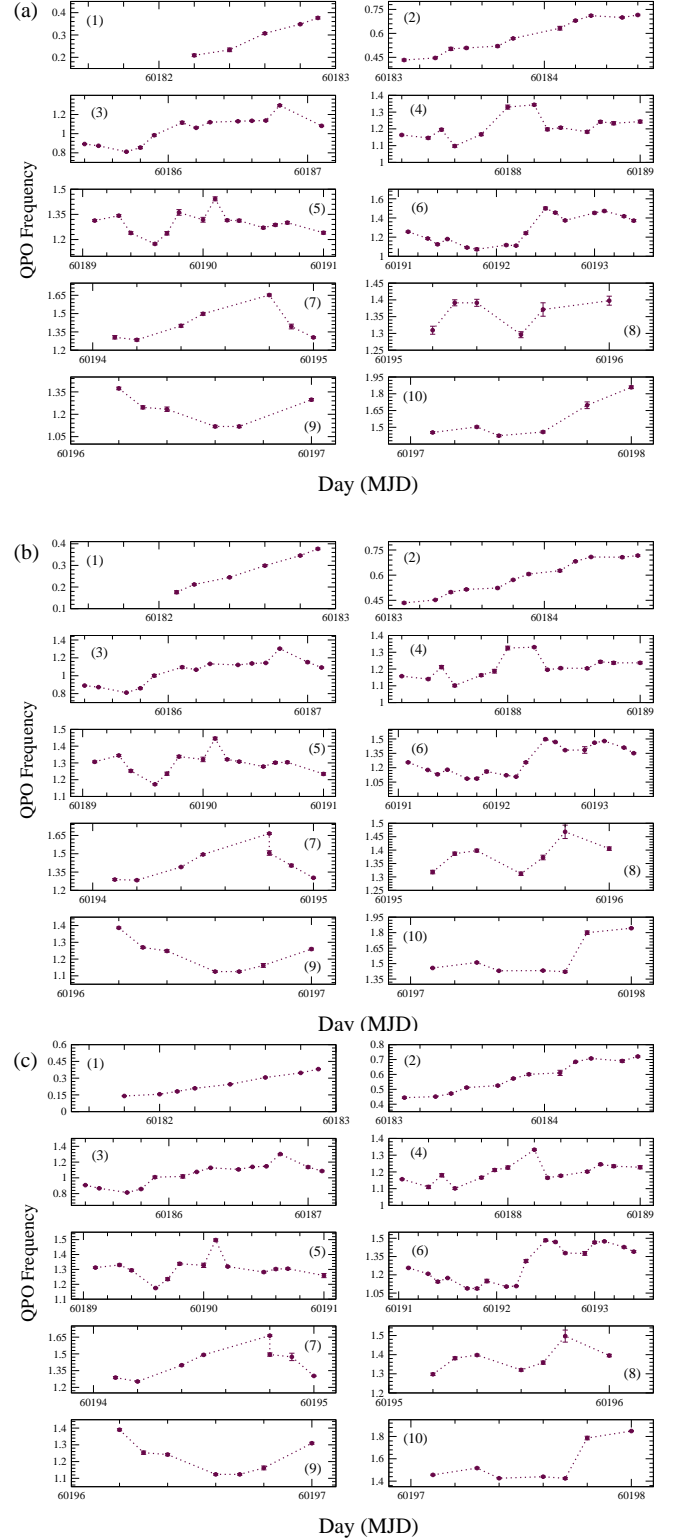


Figure 2. Evolution of QPO frequencies (Hz) with time. Here we have shown three different plots for (a) LE, (b) ME, and (c) HE instruments. Panels 1–10 in each of the three of these plots (a, b, c) represent the ν_{qpo} variation for the 10 observation IDs we used.

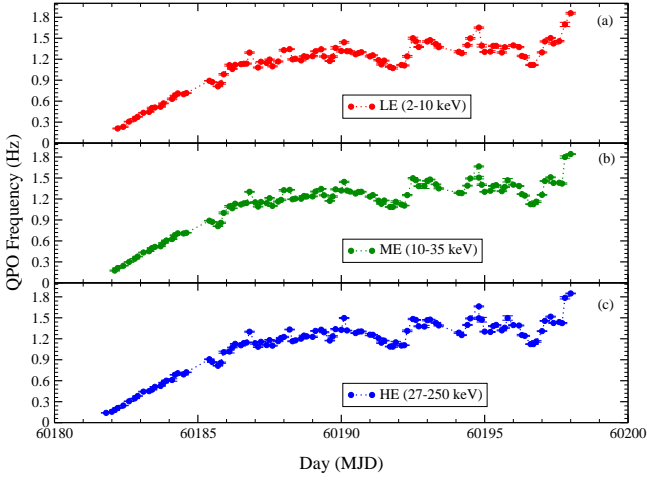


Figure 3. Evolution of QPO frequency with time during the whole period of analysis for (a) LE, (b) ME, and (c) HE.

(Fig. 4b), it increased from the onset of the analysis period for some time and then again decreased. HE band (Fig. 4c) shows a similar trend as of LE band. Since the QPO nature has already been reported in the recent paper by Yu et al. (2024), we would not put much insight into the classification of the QPO nature. However, by the values of both Q -factor and RMS, it can be said that the QPO is type-C in nature for all the exposure IDs that have been presented here.

3.2. Spectral Properties

Along with studying the timing properties, studying the spectral properties gives a clearer idea about the nature of the source. With the available Insight-HXMT data, we analyzed the source for a total of 32 exposure IDs. These exposure IDs are marked with a ‘*’ sign in the 1st column of Table 2. This source hasn’t been extensively analyzed spectrally. We perform an extensive study of this source’s spectral properties for the first few days after the onset of its outburst. We started our spectral analysis on MJD 60181.4. We have used LE+ME+HE in the 2–150 keV energy band (LE in 2–10, ME in 10–35, and HE in 35–150 keV) for our spectral fitting for all these exposure IDs.

We first fitted the data with phenomenological `diskbb` and `power-law` models. We used the multiplicative `tbabs` model to account for the interstellar absorption. Our model read as `constant*tbabs(diskbb + powerlaw)` in XSPEC. The constant is taken to normalize between three different instruments in LE, ME, and HE. We found that the fit was not statistically acceptable. There was a clear sign of the Gaussian feature in the unfolded spectrum around 5–6 keV. Also, there was a hump-like feature ~ 20 keV. Besides these features, the absorption feature was noticed below 2 keV. Thus, we refitted using the model combination as `constant*tbabs*gabs(diskbb + power-law + ga + pexrav)`. Here, the `gabs` model takes care of

Evolution of rms (%) with QPO frequency and time

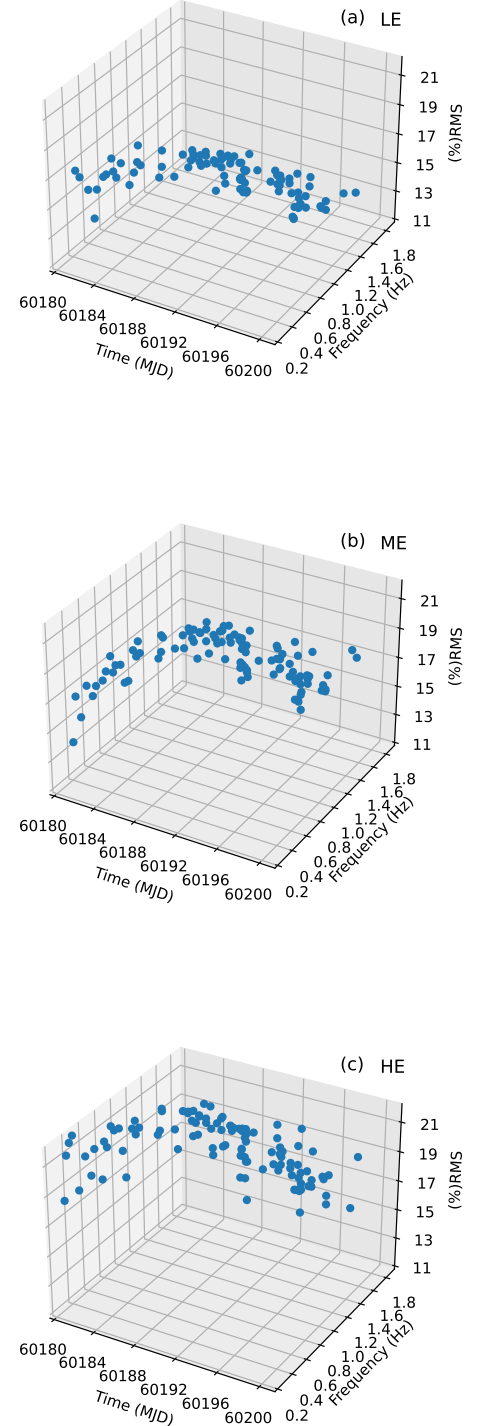


Figure 4. 3-D representation of the variation of ν_{qpo} and (%RMS) with time (MJD) for (a) LE, (b) ME, and (c) HE.

Model Fitted Insight-HXMT Spectra

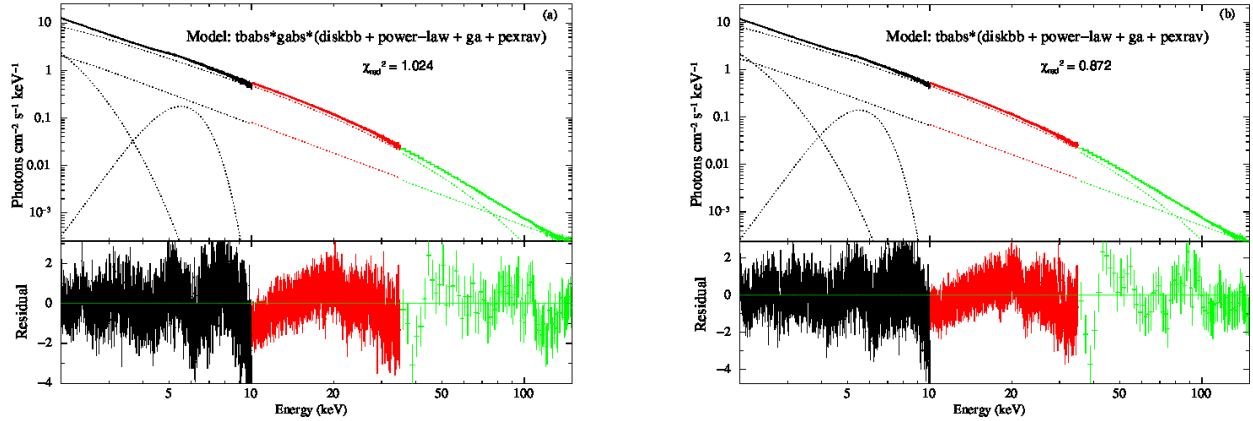


Figure 5. Model fitted spectrally analyzed unfolded spectra. (a) is for observation ID. P061433800501 (Exposure: P061433800501-20230902-01-01) for which the *gabs* model was necessary to achieve the best fit. (b) is for the observation ID. P061433800601 (exposure: P061433800601-20230904-01-01) for which the *gabs* model was not needed to achieve the best fit.

the low energy absorption feature, while the *ga* and *pexrav* models take care of the contribution from the Gaussian and hump-like nature, as mentioned above. In Fig. 5a, we show the best-fitted unfolded spectrum using this model combination for the observation ID P061433800501 (Exposure ID: P061433800501-20230902-01-01), where $\chi^2/DOF \sim 1$. After some exposure, we found that the *gabs* model was not needed anymore to achieve the best fit. Then, the model combination in XSPEC reads as `constant*tbabs(diskbb + power-law + ga + pexrav)`. In Figure 5b, we show an unfolded best-fitted spectrum using the later model combination. This is for the observation ID. P061433800601 (exposure ID: P061433800601-20230904-01-01), for which $\chi^2/DOF \sim 0.9$.

For our overall spectral analysis with the two combinations of models, we have assumed $abund = 1.0$ and $Fe_{abund} = 1.0$ in the *pexrav* model with redshift (z) = 0. From the spectral fitting, we extracted various properties of the source during the first few days of the outburst. We estimated the inner-disk temperature (T_{in}), photon index of power-law (Γ) which is the slope of the spectrum. We found that from MJD 60181.4 to 60190.0, there was an absorption feature at $\sim 1.65 - 1.95$ keV. After this day, the *gabs* model was no longer needed to achieve the best fit. The T_{in} was $\sim 0.18 \pm 0.0022$ keV at the start of the outburst and it gradually increased to $\sim 0.42 \pm 0.003$ keV on the last day of our analysis. The Γ of the *power-law* model was 2.12 ± 0.009 at the starting day. From the variation of the light curve in Figure 1, we notice that the flux was already very high at the starting date of our analysis (HXMT data was available from this date too). The value of T_{in} and Γ of *power-law* model indicates that the source has already transitioned past its hard state spectral nature and could be in an intermediate state. As the outburst progressed more, T_{in} became higher with the norm of the *diskbb* model decreased as the outburst progressed. Γ of the *power-law* model varied in the range 2.10 – 2.16 for the first few days then decreased a little and

then again slowly increased to 2.20. We found the presence of a broad Gaussian line, with the line energy varying between 5.2 – 5.75 keV. We did not link the Γ of the *pexrav* model to the Γ of the *power-law* model, as we noticed that the spectral slope was different between low and high energies. From the *pexrav* model, we estimated the slope of the spectra in the higher energy domain, along with the energy break (E_{cut}) where this slope changes. From the results listed in Table 4, we notice that the higher energy slope of the spectrum varied in the range of 0.94 – 1.9. The E_{cut} varied in the range of $\sim 20 - 32$. The $\cos(i)$ parameter varied in the range 0.05 – 0.5. The column density of H (N_H) varied in the range $0.1 - 0.35 \times 10^{22} \text{ cm}^{-2}$ during the entire duration of this analysis. In Figure 6(a-f), we show the variations of the spectral model fitted parameters with time.

3.3. Correlation between spectral and timing properties

The QPO frequency could be produced from the oscillation of the Compton corona, which could also be the origin of the hard power-law photons that extend the spectrum to very high energies. They could be correlated to each other. It has been previously seen that the QPO frequency (ν_{qpo}) and the photon index of power-law (Γ) show a positive correlation for some of the sources during their active outbursting phase (Vignarca et al. 2003; Shaposhnikov & Titarchuk 2009; Stiele et al. 2013). We also tried to find out if there are any correlations between these two properties. In Figure 7, we show the variations of the photon index with the QPO frequency for the three energy bands. Considering these points, we have found a positive correlation between Γ and ν_{qpo} . Using both the Pearson-Linear and Spearman-Rank correlation methods, we found correlation coefficients for the three energy bands as below.

	Pearson-Linear	Spearman-Rank
LE	0.65 ± 0.15	0.65 ± 0.19
ME	0.65 ± 0.15	0.65 ± 0.19
HE	0.64 ± 0.15	0.64 ± 0.19

Model Fitted Insight-HXMT Spectra

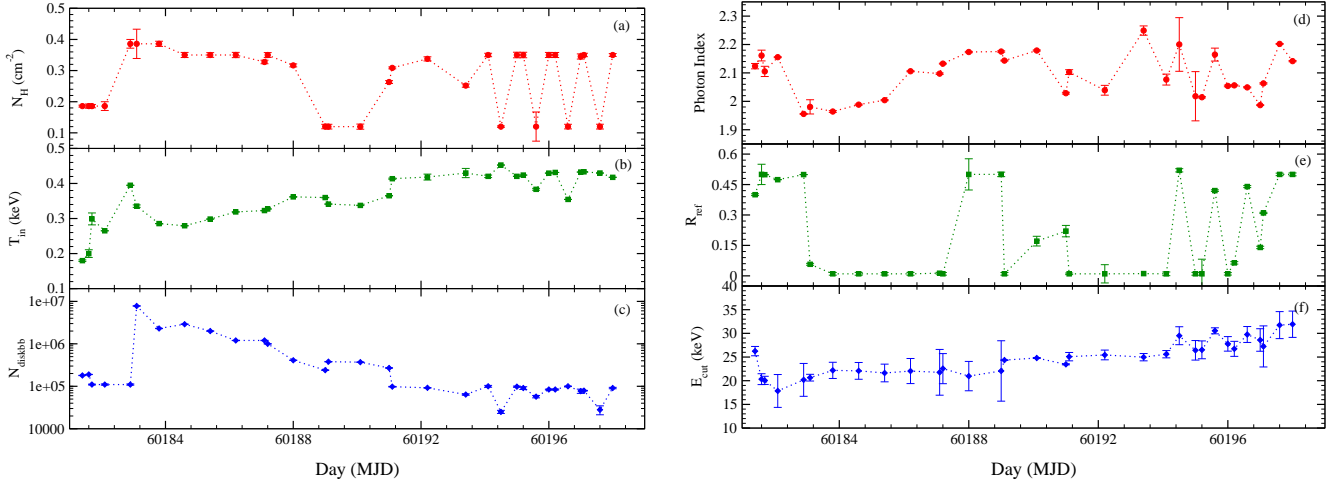


Figure 6. Variation of spectrally fitted properties (a) hydrogen column density (n_H), (b) inner-disk temperature (T_{in}), (c) diskbb normalization, (d) Photon Index (Γ), (e) reflection fraction (R_{ref}), and (f) cutoff energy (E_{cut}) with time.

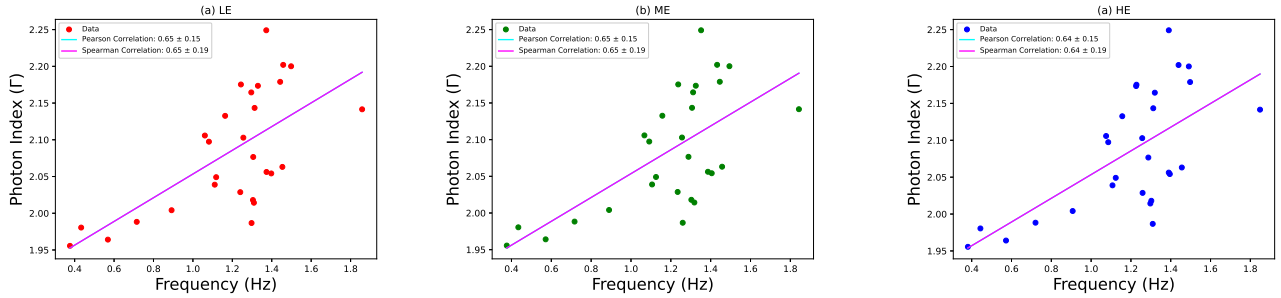
Photon Index (Γ) vs QPO frequency (ν_{qpo})

Figure 7. Variation of photon index of power-law (Γ) with QPO frequency (ν_{qpo}) for (a) LE, (b) ME, and (c) HE instruments. Here, Γ is the spectral fitted index using combined LE+ME+HE data.

4. DISCUSSIONS

The Galactic black hole Swift J1727.8-1613 was monitored daily by various X-ray satellites like NICER, NuSTAR, Insight-HXMT, etc. Multi-wavelength follow-up observations were also carried out for this source. We have taken HXMT data for both our spectral and timing analysis from MJD 60181.4 to 60198.0. The evolution of the light curve makes the outburst nature of the source a fast-rise slow decay type. After the onset of the outburst, it rose to its peak very fast within 5 days. Using the 0.01 s time-binned light curves from the three instruments of HXMT (LE, ME, and HE), we studied the source's timing properties by analyzing the light curves. Using the spectra files from these three instruments we also studied the spectral properties of this source by analyzing combined LE+ME+HE spectra in the 2 – 150 keV broad energy range.

4.1. Propagation of Shock

Quasi-periodic oscillation is one of the most important and common phenomena for stellar mass black holes. For this

newly discovered source, we analyzed light curves of a total of 342 light curves (114 for LE, ME, and HE each). However, in some of the exposures, light curves were not produced properly. There were a total of 92 exposures which commonly produced LE, ME, and HE light curves. We list those data in Table 3. Our analysis is final for 276 data. We found the presence of QPO in all of these light curves and they show rapid evolution in frequency in this short analysis period. The QPO frequency (ν_{qpo}) showed an increase in frequency within even a single day. This is one of the advantages of using Insight-HXMT as it provides multiple exposures for one observation ID which helps to study the short-scale variations of such important physical properties of the source. The evolution of the QPO frequency has been discussed broadly in the result section. It showed an increasing trend from the start of our analysis. From the variation of QPO frequency, (%RMS), and Q -factor, the nature of the QPO is designated to be type-C. Although this is a well-established topic in the literature, the origin of QPO is still a matter of debate. Many models try to explain the type-C

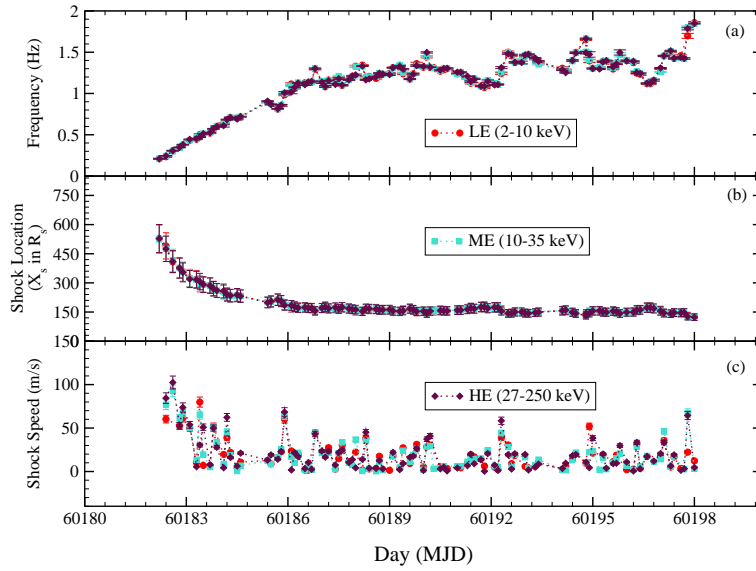


Figure 8. Variation of shock properties with time in accordance with v_{qpo} . In (a) the variation of v_{qpo} with time and in (b) and (c) we show the variations of the shock location (X_s), and shock speed (v) with time.

QPO phenomenon, e.g., the Lense-Thirring effect (Stella & Vietri 1998), accretion-ejection instability (Tagger & Pellat 1999), oscillation of the disk (Titarchuk & Osherovich 2000), the misalignment between the spin and binary rotational axis (Ingram et al. 2009, and references therein).

We would like to focus on a physical scenario that the QPOs could have originated from the shock instabilities in advective flows around black holes. Black hole accretion is transonic in which multiple sonic points could exist (Chakrabarti & Titarchuk 1995). Depending on the flow properties, there is the possibility of the formation of standing shocks (Singh et al. 2022 and references therein). The matter from the companion need not necessarily be only Keplerian. There could be a supply of matter which has angular momentum distribution deviated from the Keplerian one. This is the sub-Keplerian component. Such a lower angular momentum component of infalling matter gets accreted in a free-fall timescale. Due to the tug of war between the pressure of gravitational force and centrifugal force, this matter could virtually stop from falling onto the BH at some distance from the BH and undergo shock transition, creating a post-shock region. This approach could very well describe the spectral and temporal properties of BH, as it has been shown previously in both theoretical (Chakrabarti & Titarchuk 1995) and observational (Debnath et al. 2014; Mondal et al. 2014, Chatterjee et al. 2020, 2021, 2023) studies. The change in size of such post-shock region can describe the spectro-temporal properties during an outburst. According to Molteni et al. (1996), the oscillation in the shock region could have originated due to the presence of cooling. This was later shown in simulation works by Garain et al. (2014). The oscillation of the shock region could have originated due to the resonance condition between the cool-

ing timescale due to the Comptonization process and the infall timescale in the coronal region (see Chakrabarti et al. 2015). Additionally, it has also been observed by the authors that once the QPO sets in, it gets locked for a week or more depending on the above condition. From the expressions of infall and cooling timescales, we get that the QPO frequency (v_{qpo}) could be given as (Molteni et al. 1996; Chakrabarti & Manickam 2000; Chakrabarti et al. 2004),

$$v_{qpo} = \frac{c^3}{2GM_{BH}} \frac{1}{RX_s(X_s - 1)^{1/2}} Hz, \quad (1)$$

where c and G are the speed of light and gravitational constant respectively. M_{BH} represents the mass of the black hole, X_s is the distance of the shock, or called shock location. X_s is in the units of Schwarzschild radius ($r_s = 2GM_{BH}/c^2$). R is the ratio of matter densities in post-shock to pre-shock regions (ρ_+/ρ_-) and is known as the compression ratio. From our timing analysis, we already extracted the information about QPO frequency (v_{qpo}). Using the above relation, we estimated the shock location during the outburst. According to Chakrabarti et al. (2005), X_s could be located anywhere from 10 to 1000 r_s . The shock stays very far away $\sim 1000 r_s$ when the spectral nature of the ongoing outburst is hard and becomes smaller gradually in the process of cooling. Using the relation (1), we found that the shock was far at the start of the analysis period (Fig. 8b). It then rapidly decreased as the QPO frequency increased rapidly during the initial few days. Close to MJD 60185, when the v_{qpo} stopped its rapid increment, and the shock location started to decrease very slowly. The values of the shock location along with QPO frequency are given in Table 3. As equation (1) suggests, as the shock was bigger at the start of the outburst, the QPO frequency

was small. As it decreased rapidly due to cooling, the v_{qpo} increased rapidly. Then when the cooling was less efficient, the size of the shock changed very slowly, although decreasing. It made the v_{qpo} increase with time but not so rapidly as before.

If the time of the first exposure ID was taken to be 0, and the shock location as X_{s0} and after time t , if the shock is at X_s , then the velocity of the movement of the shock would be given by the equation (Chakrabarti et al. 2005)

$$v = \frac{X_{s0} - X_s}{t} \text{ ms}^{-1} \quad (2)$$

Using this relation, we estimated the velocity of shock. This is given in Fig. 8c. We find that the shock velocity has varied within this period. In the beginning, it attained higher values when the X_s was also larger, however decreasing rapidly. It slowed down as the shock moved inwards, along with some fluctuations. This could be due to the limitation of assuming constant velocity of the movement of the shock.

4.2. Evolution of the physical configuration and spectral nature

From the spectral properties, we have seen that the T_{in} was first low and it gradually increased. The exact opposite trend was observed for the Normalization of the `diskbb` model. The norm of `diskbb` model varies as

$$N_{diskbb} = \left(\frac{R_{in}}{D_{10}} \right)^2 \cos i \quad (3)$$

where, R_{in} , D_{10} are the inner-disk radius of the accretion disk and the distance of the source in 10 kpc unit. i is the inclination angle of the accretion disk to the observer. Considering, D_{10} and θ do not change during an outburst, the relation could be shortened like $R_{in} \sim N_{diskbb}^{1/2}$. Thus as the N_{diskbb} decreased, it means the inner edge of the disk moved closer to the black hole. This is also supported by the fact that T_{in} increased as the disk came closer.

This also supports the properties we showed from the timing analysis. The shock forms at a distance (X_s) when the sub-Keplerian matter is halted due to the counterbalance between the pressures of gravitational force and the centrifugal force. This forms the hot Compton cloud, as it becomes hot and puffed up in time. The hot Compton cloud will intercept some of those disk photons and there will be scattering in the process of inverse-Comptonization that will increase the energy of those intercepted photons and will emit them at higher energies. In this way, the Compton cloud will be cooled due to energy loss. Due to this cooling, the Compton cloud will gradually shrink in size. As it continues shrinking in size, the disk will continue to move inwards. As we have seen from the timing properties, the shock location was larger at the start of the outburst. The inner-disk radius was also higher as $R_{in} \sim N_{diskbb}^{1/2}$ and N_{diskbb} was higher. Then

cooling starts as the disk starts to approach inwards. In this way, the Compton cloud was losing energy by up-scattering and as the cooling continued, the X_s and R_{in} were both moving closer to the black hole.

Looking at the spectral parameters, and also the location of the shock, we designate that the source was already in an intermediate state at the start of our analysis period. As the outburst progressed, it was transitioning towards softer states.

From the values of the parameter $\cos(i)$ of the `pexrav` model, we find that the inclination of the disk was $> 60^\circ$, which makes this source a high inclination binary system.

The hydrogen column density (N_H) showed a variation, which is common for Galactic black hole binaries unless the system is heavily obscured, which has recently been found for the newly discovered BH Swift J151857.0-572147 (Mondal et al. 2024). The average N_H has an average value of $0.27^{+0.08}_{-0.17} \times 10^{22} \text{ cm}^{-2}$.

5. SUMMARY AND CONCLUSIONS

We have studied the timing and spectral properties of the BHC Swift J1727.8-1613 during its recent outburst in 2023. We show the evolution of the light curve along with its hardness ratio for the entire duration of the outburst using archival MAXI/GSC data. Studying the entire evolution of the outburst was not the scope of this paper. Using the Insight-HXMT data, we chose the first ten observation IDs for our analysis. We use all the exposures from those observation IDs and selective exposures for timing and spectral analysis, respectively. Using 0.01 s time-binned light curves from all three instruments of HXMT, i.e., LE, ME, and HE, we studied the QPO properties by producing a power density spectrum. The QPO properties were extracted with the use of Lorentzian model. For spectral analysis, we use LE + ME + HE spectrum files in the broad 2 – 150 keV energy band. We found that the models i) `constant*tbabs*gabs*(diskbb + power-law + gaussian + pexrav)` (for those for which `gabs` was required), ii) `constant*tbabs*(diskbb + power-law + gaussian + pexrav)` fits the spectra best. From our analysis, we conclude that:

(i) Quasi-periodic oscillations were present during the entire period of our analysis, which showed evolution in QPO frequency.

(ii) The Q -factor and RMS help designate the nature of the QPOs as type-C.

(iii) QPOs originated from the shock instabilities that was formed by matter having an angular momentum distribution deviated from the Keplerian distribution. As the shock moved inwards, the QPO frequency was observed to increase.

(iv) With the shock moving inwards, the spectral nature of the source was transitioning towards the softer states, after it started in the intermediate state at the onset of the analysis period.

(v) The spectral and temporal properties correlate to each other which makes our claim stronger about the origin of QPOs.

(vi) This source is in a high inclination binary system.

(vii) The hydrogen column density varied in the range of $0.10 - 0.35 \times 10^{22} \text{ cm}^{-2}$, which is quite common for interstellar absorption of Galactic black holes.

6. DATA AVAILABILITY

This work has made use of public data from several satellite/instrument archives and has made use of software from the HEASARC, which is developed and monitored by the Astrophysics Science Division at NASA/GSFC and the High Energy Astrophysics Division of the Smithsonian Astrophys-

ical Observatory. This work made use of the data from the Insight-HXMT mission, a project funded by the China National Space Administration (CNSA) and the Chinese Academy of Sciences (CAS).

7. ACKNOWLEDGEMENTS

KC acknowledges support from the SWIFAR postdoctoral fund of Yunnan University. SM acknowledges the Ramanujan Fellowship (# RJF/2020/000113) by SERB-DST, Govt. of India for this research. CBS is supported by the National Natural Science Foundation of China under grant no. 12073021.

REFERENCES

- Baglio, M. C., Casella, P., Testa, V., et al. 2023, *The Astronomer's Telegram*, 16225, 1
- Belloni, T., Homan, J., Casella, P., van der Klis, M., et al., 2005, *A&A*, 440, 207
- Belloni, T. M., Motta, S. E., & Muñoz-Darias, T., 2011, *Bulletin of the Astronomical Society of India*, 39, 409
- Blandford, R. D., & Payne, D. G., 1981a, *MNRAS*, 194, 1033
- Blandford, R. D., & Payne, D. G., 1981b, *MNRAS*, 194, 1041
- Bollemeijer, N., Uttley, P., Buisson, D., et al. 2023, *The Astronomer's Telegram*, 16247, 1
- Borozdin, K., Revnivtsev, M., Trudolyubov, S., Shrader, C., & Titarchuk, L., 1999, *ApJ*, 517, 367
- Bright, J., Farah, W., Fender, R., et al. 2023, *The Astronomer's Telegram*, 16228, 1
- Cao, X., Jiang, W., Meng, B., et al. 2020, *Science China Physics, Mechanics, and Astronomy*, 63, 249504
- Casella, P., Belloni, T., & Stella, L., 2005, *ApJ*, 629, 403
- Castro-Tirado, A. J., Sanchez-Ramirez, R., Caballero-Garcia, M. D., et al. 2023, *The Astronomer's Telegram*, 16208, 1
- Chakrabarti, S., & Titarchuk, L. G., 1995, *ApJ*, 455, 623
- Chakrabarti, S. K., & Manickam, S. G., 2000, *ApJ*, 531, L41
- Chakrabarti, S. K., Acharya, K., & Molteni, D., 2004, *A&A*, 421, 1
- Chakrabarti, S. K., Nandi, A., Debnath, D., Sarkar, R., & Datta, B. G., 2005, preprint (arXiv:astro-ph/0508024)
- Chakrabarti, S. K., Debnath, D., Nandi, A., & Pal, P. S., 2008, *A&A*, 489, L41
- Chakrabarti, S. K., Mondal, S., & Debnath, D., 2015, *MNRAS*, 452, 3451
- Chakrabarti, S. K., Debnath, D., & Nagarkoti, S., 2019, *AdSpR*, 64, 3749
- Chatterjee, K., Debnath, D., Chatterjee, D., Jana, A., Chakrabarti, S. K., 2020, *MNRAS*, 493, 2452
- Chatterjee, K., Debnath, D., Chatterjee, D., Jana, A., et al., 2021, *Ap&SS*, 366, 63
- Chatterjee, K., Debnath, D., Bhowmick, R., Nath, S. K., & Chatterjee, D., 2022, *MNRAS*, 510, 1128
- Chatterjee, K., Debnath, D., Nath, S. K., Chang, S.-K., 2023, *ApJ*, 965, 55
- Chatterjee, K., Debnath, D., Nath, S. K., & Chang, H. -K., 2023, *ApJ*, 965, 55
- Chen, Y., Cui, W., Li, W., et al. 2020, *Science China Physics, Mechanics, and Astronomy*, 63, 249505
- Debnath, D., Chakrabarti, S.K., & Nandi, A., 2010, *A&A*, 520, A98
- Debnath, D., Chakrabarti, S. K., & Mondal, S., 2014, *MNRAS*, 440, L121
- Debnath, D., Nath, S. K., Chatterjee, D., Chatterjee, K., Sen, K., Chang, H. -K., 2023, *The Astronomer's Telegram*, 16287, 1
- Draghis, P. A., Miller, J. M., Homan, J., et al. 2023, *The Astronomer's Telegram*, 16219, 1
- Fabian, A. C., Rees, M. J., Stella, L., & White, N. E. 1989, *MNRAS*, 238, 729
- Garain, S., Ghosh, H., & Chakrabarti, S. K., 2014, *MNRAS*, 437, 1329
- Garcia, J., & Kallman, T. R. 2010, *ApJ*, 718, 695
- George, I. M., & Fabian, A. C. 1991, *MNRAS*, 249, 352
- Guilbert, P. W., & Rees, M. J. 1988, *MNRAS*, 233, 475
- Haardt, F., & Maraschi, L., 1993, *ApJ*, 413, 507
- Homan, J., Wijnands, R., van der Klis, M., Belloni, T., van Paradijs, J., KleinWolt, M., Fender, R., & Mendez, M., 2001, *ApJS*, 132, 377
- Ingram, A., Done, C., & Fragile, P. C., 2009, *MNRAS*, 397, L101
- Ingram, A., Ewing, M., Marinucci, A., et al. 2023, *MNRAS*, doi: 10.1093/mnras/stad2625
- Jana, A., Debnath, D., Chakrabarti, S. K., Mondal, S., & Molla, A. A., 2016, *ApJ*, 819, 107
- Kennea, J. A. & Swift Team 2023, *GCN*, 34540, 1
- King, A. R., & Ritter, H., 1998, *MNRAS*, 293, L42
- Lightman, A. P., & White, T. R. 1988, *ApJ*, 335, 57
- Liu, C., Zhang, Y., Li, X., et al. 2020, *Science China Physics, Mechanics, and Astronomy*, 63, 249503

- Liu, H. Y., Li, D. Y., Pan, H. W., et al. 2023, *The Astronomer's Telegram*, 16210, 1
- Mata Sanchez, D., Munoz-Darias, T., Armas Padilla, M., Casares, J., & Torres, M. A. P., 2024, *A&A*, 682, L1
- Matsuoka, M., Kawasaki, K., Ueno, S., et al. 2009, *PASJ*, 61, 999
- Mereminskiy, I., Lutovinov, A., Molkov, S., et al. 2023, *MNRAS*, submitted, arXiv:2310.06697, doi: 10.48550/arXiv.2310.06697
- Miller-Jones, J. C. A., Sivakoff, G. R., Bahramian, A., & Russell, T. D. 2023, *The Astronomer's Telegram*, 16211, 1
- Molteni, D., Sponholz, H., & Chakrabarti, S. K., 1996, *ApJ*, 457, 805
- Mondal, S., Debnath, D., & Chakrabarti, S. K., 2014, *ApJ*, 786, 4
- Mondal, S., Suribhatla, S. P., Chatterjee, K., & Singh, C. B., 2024, *JHEAP*, (preprint: arXiv:2404.09643)
- Mondal, S., 2020, *Advances in Space Research*, 65, 693
- Munoz-Darias, T., Motta, S., & Belloni, T. M., 2011, *MNRAS*, 410, 679
- Nandi, A., Das, S., Majumder, S., et al., 2024, (preprint:arXiv:2404.17160)
- Negoro, H., Serino, M., Nakajima, M., et al. 2023b, *The Astronomer's Telegram*, 16205, 1
- Novikov, I. D., & Thorne, K. S., 1973, in *Black Holes (Les Astres Occlus)*. pp 343–450
- O'Connor, B., Hare, J., Younes, G., et al. 2023, *The Astronomer's Telegram*, 16207, 1
- Palmer, D. M., & Parsotan, T. M. 2023, *The Astronomer's Telegram*, 16215, 1
- Payne, D. G., & Blandford, R. D., 1981, *MNRAS*, 196, 781
- Pozdniakov, L. A., Sobol, I. M., & Sunyaev, R. A., 1979, *A&A*, 75, 214
- Psaltis, D., & Lamb, F. K., 1997, *ApJ*, 488, 881
- Psaltis, D., 2001, *ApJ*, 555, 786
- Remillard, R. A., & McClintock, J. E., 2006, *ARA&A*, 44, 49
- Riaz, A., Szanecki, M., Niedzwiecki, A., Ayzenberg, D., & Bambi, C., 2021, *ApJ*, 910, 49
- Ross, R. R., & Fabian, A. C. 2005, *MNRAS*, 358, 211
- Shakura, N. I., & Sunyaev, R. A., 1973, *A&A*, 24, 337
- Shaposhnikov, N., & Titarchuk, L., 2009, *ApJ*, 699, 453
- Singh, C. B., Mondal, S., & Garofalo, D., 2022, *MNRAS*, 510, 807
- Stiele, H., Belloni, T. M., Kalemci, E., & Motta, S., 2013, *MNRAS*, 429, 2655
- Stella, L., & Vietri, M., 1998, *ApJ*, 492, L59
- Stella, L., Vietri, M., & Morsink, S. M., 1999, *ApJ*, 524, L63
- Sunyaev, R. A., & Titarchuk, L. G., 1980, *A&A*, 500, 167
- Sunyaev, R. A., & Titarchuk, L. G., 1985, *A&A*, 143, 374
- Sunyaev, R. A., Mereminskiy, I. A., Molkov, S. V., et al. 2023, *The Astronomer's Telegram*, 16217, 1
- Svoboda, J., Dovciak, M., Steiner, F., Kaaret, P., et al., 2024 (arxiv preprint)
- Tagger, M., & Pellat, R., 1999, *A&A*, 349, 1003
- Tetarenko, B. E., Sivakoff, G. R., Heinke, C. O., & Gladstone, J. C., 2016, *ApJS*, 222, 15
- Titarchuk, L., 1994, *ApJ*, 434, 570
- Titarchuk, L., Lapidus, I., & Muslimov, A., 1998, *ApJ*, 499, 315
- Titarchuk, L., & Osherovich, V., 2000, *ApJ*, 542, L111
- van der Klis, M., 1989, *Annu. Rev. Astron. Astrophys.*, 27, 517
- van der Klis, M., 1994, *ApJS*, 92, 511
- Veledina, A., Poutanen, J., & Ingram, A. 2013, *ApJ*, 778, 165, doi: 10.1088/0004-637X/778/2/165
- Wang, Y. D., & Bellm, E. C. 2023, *The Astronomer's Telegram*, 16209, 1
- White N. E., Nagase F., Parmar A. N., 1995, in *X-ray Binaries*. pp 1–57
- Williams-Baldwin, D., Motta, S., Rhodes, L., et al. 2023, *The Astronomer's Telegram*, 16231, 1
- Vignarca, F., Migliari, S., Belloni, T., Psaltis, D., & van der Klis, M., 2003, *A&A*, 397, 729
- Yu, W., Bu, Q.-C., Zhang, S.-N., Liu, H.-X., Zhang, L., et al., 2024, *MNRAS* (arXiv preprint)
- Zdziarski, A. A., Zycki, P. T., Svensson, R., & Boldt, E., 1993, *ApJ*, 405, 125
- Zhang, S., Lu, F. J., Zhang, S. N., & Li, T. P. 2014, in *Society of Photo-Optical Instrumentation Engineers (SPIE) Conference Series*, Vol. 9144, *Space Telescopes and Instrumentation 2014: Ultraviolet to Gamma Ray*, ed. T. Takahashi, J.-W. A. den Herder, & M. Bautz, 914421
- Zhang, S. -N., et al., 2020, *Science China Physics, Mechanics, and Astronomy* 63, 249502
- Życki, P. T., Done, C., & Smith, D. A., 1999, *MNRAS*, 309, 561

Table 2. Start and Stop Time of all the HXMT Exposures

Exposure ID (1)	UT Start (2)	MJD Start (3)	UT Stop (4)	MJD Stop (5)	Average MJD (6)
P061433800101-20230825-01-01*	2023-08-25	60181.3411	2023-08-25	60181.4980	60181.4
P061433800102-20230825-01-01*	2023-08-25	60181.4980	2023-08-25	60181.6301	60181.6
P061433800103-20230825-01-01*	2023-08-25	60181.6301	2023-08-25	60181.7622	60181.7
P061433800104-20230825-01-01	2023-08-25	60181.7622	2023-08-25	60181.8944	60181.8
P061433800105-20230825-01-01	2023-08-25	60181.8944	2023-08-26	60182.0265	60182.0
P061433800106-20230826-02-01*	2023-08-26	60182.0265	2023-08-26	60182.1586	60182.1
P061433800107-20230826-02-01	2023-08-26	60182.1586	2023-08-26	60182.2842	60182.2
P061433800108-20230826-02-01	2023-08-26	60182.2842	2023-08-26	60182.4229	60182.4
P061433800110-20230826-02-01	2023-08-26	60182.5551	2023-08-26	60182.6872	60182.6
P061433800111-20230826-02-01	2023-08-26	60182.6872	2023-08-26	60182.8193	60182.8
P061433800112-20230826-02-01*	2023-08-26	60182.8193	2023-08-26	60182.9515	60182.9
P061433800113-20230826-02-01	2023-08-26	60182.9515	2023-08-27	60183.0598	60183.0
P061433800201-20230827-01-01*	2023-08-27	60183.0597	2023-08-27	60183.2029	60183.1
P061433800202-20230827-01-01	2023-08-27	60183.2029	2023-08-27	60183.3450	60183.3
P061433800203-20230827-01-01	2023-08-27	60183.3450	2023-08-27	60183.4800	60183.4
P061433800204-20230827-01-01	2023-08-27	60183.4800	2023-08-27	60183.6122	60183.5
P061433800205-20230827-01-01	2023-08-27	60183.6122	2023-08-27	60183.7443	60183.7
P061433800206-20230827-01-01*	2023-08-27	60183.7443	2023-08-27	60183.8764	60183.8
P061433800207-20230827-01-01	2023-08-27	60183.8764	2023-08-28	60184.0086	60183.9
P061433800208-20230828-02-01	2023-08-28	60184.0086	2023-08-28	60184.1407	60184.1
P061433800209-20230828-02-01	2023-08-28	60184.1407	2023-08-28	60184.2662	60184.2
P061433800210-20230828-02-01	2023-08-28	60184.2662	2023-08-28	60184.4050	60184.3
P061433800211-20230828-02-01	2023-08-28	60184.4050	2023-08-28	60184.5371	60184.5
P061433800212-20230828-02-01*	2023-08-28	60184.5371	2023-08-28	60184.6494	60184.6
P061433800301-20230829-01-01*	2023-08-29	60185.3075	2023-08-29	60185.4621	60185.4
P061433800302-20230829-01-01	2023-08-29	60185.4621	2023-08-29	60185.5942	60185.5
P061433800303-20230829-01-01	2023-08-29	60185.5942	2023-08-29	60185.7264	60185.7
P061433800304-20230829-01-01	2023-08-29	60185.7264	2023-08-29	60185.8585	60185.8
P061433800305-20230829-01-01	2023-08-29	60185.8585	2023-08-29	60185.9906	60185.9
P061433800306-20230829-01-01	2023-08-29	60185.9906	2023-08-30	60186.1228	60186.1
P061433800307-20230830-02-01*	2023-08-30	60186.1228	2023-08-30	60186.2481	60186.2
P061433800308-20230830-02-01	2023-08-30	60186.2481	2023-08-30	60186.3866	60186.3
P061433800309-20230830-02-01	2023-08-30	60186.3866	2023-08-30	60186.5192	60186.5
P061433800310-20230830-02-01	2023-08-30	60186.5192	2023-08-30	60186.6513	60186.6
P061433800311-20230830-02-01	2023-08-30	60186.6513	2023-08-30	60186.7835	60186.7
P061433800312-20230830-02-01	2023-08-30	60186.7835	2023-08-30	60186.9156	60186.8
P061433800313-20230830-02-01	2023-08-30	60186.9156	2023-08-31	60187.0478	60187.0
P061433800314-20230831-03-01*	2023-08-31	60187.0478	2023-08-31	60187.1589	60187.1
P061433800401-20230831-01-01*	2023-08-31	60187.1589	2023-08-31	60187.3083	60187.2
P061433800402-20230831-01-01	2023-08-31	60187.3083	2023-08-31	60187.4442	60187.4

Continued on next page

Table 2 – continued from previous page

Exposure ID (1)	UT Start (2)	MJD Start (3)	UT Stop (4)	MJD Stop (5)	Average MJD (6)
P061433800403-20230831-01-01	2023-08-31	60187.4442	2023-08-31	60187.5763	60187.5
P061433800404-20230831-01-01	2023-08-31	60187.5763	2023-08-31	60187.7084	60187.6
P061433800405-20230831-01-01	2023-08-31	60187.7084	2023-08-31	60187.8406	60187.8
P061433800406-20230831-01-01	2023-08-31	60187.8406	2023-08-31	60187.9727	60187.9
P061433800407-20230831-01-01*	2023-08-31	60187.9727	2023-09-01	60188.1049	60188.0
P061433800408-20230901-02-01	2023-09-01	60188.1049	2023-09-01	60188.2298	60188.2
P061433800409-20230901-02-01	2023-09-01	60188.2298	2023-09-01	60188.3682	60188.3
P061433800410-20230901-02-01	2023-09-01	60188.3682	2023-09-01	60188.5013	60188.4
P061433800411-20230901-02-01	2023-09-01	60188.5013	2023-09-01	60188.6334	60188.6
P061433800412-20230901-02-01	2023-09-01	60188.6334	2023-09-01	60188.7656	60188.7
P061433800413-20230901-02-01	2023-09-01	60188.7656	2023-09-01	60188.8977	60188.8
P061433800414-20230901-02-01*	2023-09-01	60188.8977	2023-09-02	60189.0765	60189.0
P061433800501-20230902-01-01*	2023-09-02	60189.0765	2023-09-02	60189.2206	60189.1
P061433800502-20230902-01-01	2023-09-02	60189.2206	2023-09-02	60189.3590	60189.3
P061433800503-20230902-01-01	2023-09-02	60189.3590	2023-09-02	60189.4924	60189.4
P061433800504-20230902-01-01	2023-09-02	60189.4924	2023-09-02	60189.6245	60189.6
P061433800505-20230902-01-01	2023-09-02	60189.6245	2023-09-02	60189.7567	60189.7
P061433800506-20230902-01-01	2023-09-02	60189.7567	2023-09-02	60189.8888	60189.8
P061433800507-20230902-01-01	2023-09-02	60189.8888	2023-09-03	60190.0209	60190.0
P061433800508-20230903-02-01*	2023-09-03	60190.0209	2023-09-03	60190.1531	60190.1
P061433800509-20230903-02-01	2023-09-03	60190.1531	2023-09-03	60190.2806	60190.2
P061433800510-20230903-02-01	2023-09-03	60190.2806	2023-09-03	60190.4174	60190.3
P061433800511-20230903-02-01	2023-09-03	60190.4174	2023-09-03	60190.5495	60190.5
P061433800512-20230903-02-01	2023-09-03	60190.5495	2023-09-03	60190.6817	60190.6
P061433800513-20230903-02-01	2023-09-03	60190.6817	2023-09-03	60190.8138	60190.7
P061433800514-20230903-02-01	2023-09-03	60190.8138	2023-09-03	60190.9460	60190.9
P061433800515-20230903-02-01*	2023-09-03	60190.9460	2023-09-04	60191.0601	60191.0
P061433800601-20230904-01-01*	2023-09-04	60191.0601	2023-09-04	60191.2022	60191.1
P061433800602-20230904-01-01	2023-09-04	60191.2022	2023-09-04	60191.3406	60191.3
P061433800603-20230904-01-01	2023-09-04	60191.3406	2023-09-04	60191.4746	60191.4
P061433800604-20230904-01-01	2023-09-04	60191.4746	2023-09-04	60191.6067	60191.5
P061433800605-20230904-01-01	2023-09-04	60191.6067	2023-09-04	60191.7389	60191.7
P061433800606-20230904-01-01	2023-09-04	60191.7389	2023-09-04	60191.8710	60191.8
P061433800607-20230904-01-01	2023-09-04	60191.8710	2023-09-05	60192.0032	60191.9
P061433800608-20230905-02-01	2023-09-05	60192.0032	2023-09-05	60192.1353	60192.1
P061433800609-20230905-02-01*	2023-09-05	60192.1353	2023-09-05	60192.2621	60192.2
P061433800610-20230905-02-01	2023-09-05	60192.2621	2023-09-05	60192.3996	60192.3
P061433800611-20230905-02-01	2023-09-05	60192.3996	2023-09-05	60192.5318	60192.5
P061433800612-20230905-02-01	2023-09-05	60192.5318	2023-09-05	60192.6639	60192.6
P061433800613-20230905-02-01	2023-09-05	60192.6639	2023-09-05	60192.7961	60192.7
P061433800614-20230905-02-01	2023-09-05	60192.7961	2023-09-05	60192.9283	60192.9
P061433800615-20230905-02-01	2023-09-05	60192.9283	2023-09-06	60193.0604	60193.0
P061433800616-20230906-03-01	2023-09-06	60193.0604	2023-09-06	60193.1926	60193.1

Continued on next page

Table 2 – continued from previous page

Exposure ID (1)	UT Start (2)	MJD Start (3)	UT Stop (4)	MJD Stop (5)	Average MJD (6)
P061433800617-20230906-03-01	2023-09-06	60193.1926	2023-09-06	60193.3222	60193.3
P061433800618-20230906-03-01*	2023-09-06	60193.3222	2023-09-06	60193.4448	60193.4
P061433800801-20230907-01-01*	2023-09-07	60194.0351	2023-09-07	60194.1745	60194.1
P061433800802-20230907-01-01	2023-09-07	60194.1745	2023-09-07	60194.3130	60194.2
P061433800803-20230907-01-01	2023-09-07	60194.3130	2023-09-07	60194.4481	60194.4
P061433800804-20230907-01-01*	2023-09-07	60194.4481	2023-09-07	60194.5802	60194.5
P061433800805-20230907-01-01	2023-09-07	60194.7124	2023-09-07	60194.8446	60194.8
P061433800806-20230907-01-01	2023-09-07	60194.7124	2023-09-07	60194.8446	60194.8
P061433800807-20230907-01-01	2023-09-07	60194.8446	2023-09-07	60194.9767	60194.9
P061433800808-20230907-01-01*	2023-09-07	60194.9767	2023-09-08	60195.0927	60195.0
P061433800901-20230908-01-01*	2023-09-08	60195.0927	2023-09-08	60195.2343	60195.2
P061433800902-20230908-01-01	2023-09-08	60195.2343	2023-09-08	60195.3732	60195.3
P061433800903-20230908-01-01	2023-09-08	60195.3732	2023-09-08	60195.5054	60195.4
P061433800904-20230908-01-01*	2023-09-08	60195.5054	2023-09-08	60195.6375	60195.6
P061433800905-20230908-01-01	2023-09-08	60195.6375	2023-09-08	60195.7697	60195.7
P061433800906-20230908-01-01	2023-09-08	60195.7697	2023-09-08	60195.9019	60195.8
P061433800907-20230908-01-01*	2023-09-08	60195.9019	2023-09-09	60196.0841	60196.0
P061433801001-20230909-01-01*	2023-09-09	60196.0841	2023-09-09	60196.2251	60196.2
P061433801002-20230909-01-01	2023-09-09	60196.2251	2023-09-09	60196.3645	60196.3
P061433801003-20230909-01-01	2023-09-09	60196.3645	2023-09-09	60196.4967	60196.4
P061433801004-20230909-01-01*	2023-09-09	60196.4967	2023-09-09	60196.6288	60196.6
P061433801005-20230909-01-01	2023-09-09	60196.6288	2023-09-09	60196.7610	60196.7
P061433801006-20230909-01-01	2023-09-09	60196.7610	2023-09-09	60196.8932	60196.8
P061433801007-20230909-01-01*	2023-09-09	60196.8932	2023-09-10	60197.0754	60197.0
P061433801101-20230910-01-01*	2023-09-10	60197.0754	2023-09-10	60197.2158	60197.1
P061433801102-20230910-01-01	2023-09-10	60197.2158	2023-09-10	60197.3558	60197.3
P061433801103-20230910-01-01	2023-09-10	60197.3558	2023-09-10	60197.4879	60197.4
P061433801104-20230910-01-01*	2023-09-10	60197.4879	2023-09-10	60197.6201	60197.6
P061433801105-20230910-01-01	2023-09-10	60197.6201	2023-09-10	60197.7523	60197.7
P061433801106-20230910-01-01	2023-09-10	60197.7523	2023-09-10	60197.8845	60197.8
P061433801107-20230910-01-01*	2023-09-10	60197.8845	2023-09-11	60198.0667	60198.0

Column 1 represents the Exposure IDs, taken for this complete analysis.

Column 2 and 4 represent the time (UT) of start and end of those exposures.

Column 3 and 5 represent the start and end MJDs of those exposures respectively.

Column 6 represents the average MJD for those exposure IDs.

Table 3. Properties estimated using timing analysis

Time (MJD)	QPO Frequency (Hz)			Q-Value			RMS			Shock Location (X_s)		
	LE	ME	HE	LE	ME	HE	LE	ME	HE	LE	ME	HE
(1)	(2)	(3)	(4)	(5)	(6)	(7)	(8)	(9)	(10)	(11)	(12)	(13)
2.19	0.20 ± 0.005	0.21 ± 0.003	0.20 ± 0.004	2.2 ± 0.5	3.6 ± 0.6	2.5 ± 0.6	18.0 ± 2.8	17.8 ± 2.2	23.3 ± 3.3	528.1 ± 72.5	523.5 ± 71.9	527.8 ± 72.5
2.39	0.23 ± 0.008	0.24 ± 0.002	0.24 ± 0.002	2.6 ± 0.7	4.4 ± 0.7	5.0 ± 0.7	17.5 ± 3.1	16.3 ± 1.8	19.7 ± 2.0	490.4 ± 67.3	475.3 ± 65.3	474.9 ± 65.2
2.60	0.30 ± 0.004	0.29 ± 0.004	0.30 ± 0.003	4.2 ± 0.7	3.2 ± 0.5	4.3 ± 0.6	16.3 ± 2.1	18.2 ± 2.0	21.7 ± 2.3	408.5 ± 56.1	416.1 ± 57.1	409.5 ± 56.2
2.80	0.34 ± 0.002	0.34 ± 0.003	0.34 ± 0.002	8.4 ± 1.6	5.5 ± 0.8	6.8 ± 1.4	14.2 ± 2.0	17.4 ± 1.8	20.3 ± 2.8	375.7 ± 51.6	377.8 ± 51.9	376.6 ± 51.7
2.89	0.37 ± 0.005	0.37 ± 0.003	0.38 ± 0.003	4.7 ± 1.0	5.2 ± 0.9	4.8 ± 0.7	16.1 ± 2.6	17.9 ± 2.4	21.9 ± 2.5	356.8 ± 49.0	356.7 ± 49.0	354.0 ± 48.6
3.10	0.43 ± 0.006	0.43 ± 0.005	0.44 ± 0.005	4.8 ± 1.0	4.6 ± 0.7	6.5 ± 0.7	16.8 ± 2.4	18.1 ± 2.1	19.7 ± 1.4	324.9 ± 44.6	324.2 ± 44.5	319.7 ± 43.9
3.30	0.44 ± 0.005	0.45 ± 0.002	0.45 ± 0.002	5.1 ± 1.0	7.0 ± 0.4	6.8 ± 0.4	16.9 ± 2.4	18.7 ± 1.2	22.2 ± 1.4	318.6 ± 43.7	315.7 ± 43.3	316.3 ± 43.4
3.39	0.50 ± 0.009	0.49 ± 0.005	0.47 ± 0.004	4.0 ± 0.7	4.4 ± 0.6	6.3 ± 1.2	17.8 ± 2.3	19.5 ± 2.0	21.8 ± 3.0	294.1 ± 40.4	295.8 ± 40.6	306.9 ± 42.1
3.50	0.50 ± 0.005	0.51 ± 0.005	0.51 ± 0.005	5.8 ± 1.1	6.0 ± 1.0	5.3 ± 0.9	16.9 ± 2.2	18.4 ± 2.1	23.0 ± 3.2	291.9 ± 40.1	289.5 ± 39.7	290.6 ± 39.9
3.69	0.52 ± 0.006	0.52 ± 0.004	0.52 ± 0.004	6.1 ± 0.9	5.6 ± 0.7	5.7 ± 0.6	16.5 ± 1.9	18.9 ± 1.6	22.7 ± 1.8	287.6 ± 39.5	286.4 ± 39.3	285.7 ± 39.2
3.80	0.56 ± 0.005	0.57 ± 0.004	0.57 ± 0.004	4.7 ± 0.7	6.7 ± 0.9	6.2 ± 0.8	17.2 ± 2.1	18.7 ± 1.8	22.6 ± 2.2	271.0 ± 37.2	270.0 ± 37.1	269.8 ± 37.0
4.10	0.63 ± 0.01	0.62 ± 0.006	0.61 ± 0.021	6.4 ± 2.7	8.7 ± 2.4	3.0 ± 0.9	15.5 ± 5.0	17.5 ± 3.8	19.3 ± 4.0	252.5 ± 34.7	254.0 ± 34.9	258.5 ± 35.5
4.19	0.67 ± 0.004	0.68 ± 0.003	0.68 ± 0.004	7.1 ± 1.0	6.5 ± 0.8	7.4 ± 1.1	16.2 ± 1.6	19.3 ± 1.7	22.3 ± 2.4	240.5 ± 33.0	240.0 ± 32.9	239.4 ± 32.9
4.30	0.71 ± 0.005	0.70 ± 0.003	0.70 ± 0.003	6.2 ± 0.8	7.2 ± 0.7	6.5 ± 0.6	16.8 ± 1.6	18.8 ± 1.4	22.7 ± 1.6	233.5 ± 32.0	234.1 ± 32.1	234.2 ± 32.1
4.50	0.69 ± 0.004	0.70 ± 0.004	0.69 ± 0.009	5.9 ± 0.2	4.1 ± 0.4	5.9 ± 0.5	18.0 ± 1.1	19.8 ± 1.5	21.9 ± 2.5	236.0 ± 32.4	234.4 ± 32.2	238.1 ± 32.7
4.60	0.71 ± 0.004	0.71 ± 0.004	0.72 ± 0.004	6.7 ± 1.0	7.2 ± 0.7	6.8 ± 0.8	16.6 ± 1.9	19.0 ± 1.6	22.3 ± 2.1	232.6 ± 31.9	232.2 ± 31.9	231.4 ± 31.8
5.39	0.89 ± 0.003	0.88 ± 0.003	0.90 ± 0.005	7.7 ± 0.2	6.3 ± 0.5	5.3 ± 0.5	17.0 ± 0.8	19.7 ± 1.2	22.9 ± 1.8	200.7 ± 27.5	201.0 ± 27.6	198.4 ± 27.2
5.50	0.87 ± 0.004	0.87 ± 0.004	0.86 ± 0.004	7.1 ± 0.8	7.2 ± 0.7	6.8 ± 0.8	16.0 ± 1.5	18.6 ± 1.5	21.7 ± 2.0	203.5 ± 27.9	203.7 ± 28.0	204.5 ± 28.1
5.69	0.81 ± 0.004	0.81 ± 0.003	0.81 ± 0.003	6.4 ± 0.9	7.4 ± 0.8	7.1 ± 0.8	15.6 ± 1.7	18.5 ± 1.6	21.6 ± 1.9	213.7 ± 29.3	213.8 ± 29.3	213.3 ± 29.3
5.89	0.98 ± 0.01	1.00 ± 0.011	1.00 ± 0.011	7.0 ± 1.3	6.0 ± 1.1	6.3 ± 1.4	14.9 ± 2.1	18.4 ± 2.7	21.3 ± 3.4	188.0 ± 25.8	185.8 ± 25.5	185.0 ± 25.4
6.10	1.11 ± 0.01	1.09 ± 0.011	1.01 ± 0.022	6.9 ± 1.4	6.8 ± 1.0	9.7 ± 4.4	15.8 ± 16.	18.1 ± 2.3	19.9 ± 6.8	172.9 ± 23.7	175.0 ± 24.0	183.8 ± 25.2
6.19	1.06 ± 0.005	1.06 ± 0.004	1.07 ± 0.004	7.4 ± 0.8	7.7 ± 0.6	6.5 ± 0.5	16.2 ± 1.3	19.1 ± 1.2	22.3 ± 1.5	178.8 ± 24.5	178.1 ± 24.4	177.2 ± 24.3
6.30	1.11 ± 0.005	1.13 ± 0.004	1.12 ± 0.004	8.6 ± 1.4	6.4 ± 0.5	6.5 ± 0.5	15.1 ± 1.7	19.3 ± 1.2	21.9 ± 1.4	172.5 ± 23.7	171.2 ± 23.5	171.7 ± 23.6
6.50	1.12 ± 0.006	1.12 ± 0.004	1.10 ± 0.009	6.3 ± 0.6	7.0 ± 0.5	5.5 ± 0.9	15.6 ± 1.3	19.2 ± 1.2	22.2 ± 2.9	171.5 ± 23.5	172.3 ± 23.6	173.8 ± 23.8
6.60	1.13 ± 0.005	1.13 ± 0.005	1.13 ± 0.005	5.8 ± 0.5	7.2 ± 0.7	6.3 ± 0.5	16.3 ± 1.2	18.7 ± 1.4	21.4 ± 1.5	171.0 ± 23.5	170.7 ± 23.4	170.5 ± 23.4
6.80	1.29 ± 0.009	1.30 ± 0.005	1.30 ± 0.007	8.7 ± 1.5	9.8 ± 1.2	8.9 ± 1.2	15.2 ± 2.3	18.7 ± 1.9	21.0 ± 2.3	156.5 ± 21.5	155.9 ± 21.4	156.0 ± 21.4
7.10	1.08 ± 0.007	1.09 ± 0.006	1.08 ± 0.009	6.6 ± 0.9	6.5 ± 0.8	6.5 ± 0.9	16.1 ± 1.6	18.7 ± 1.8	20.7 ± 2.3	176.5 ± 24.2	175.4 ± 24.1	176.0 ± 24.1
7.19	1.16 ± 0.004	1.15 ± 0.003	1.15 ± 0.003	6.4 ± 0.5	7.0 ± 0.4	6.8 ± 0.4	15.9 ± 1.0	19.1 ± 1.0	21.8 ± 1.2	168.1 ± 23.1	168.7 ± 23.1	168.8 ± 23.2
7.39	1.14 ± 0.006	1.14 ± 0.004	1.11 ± 0.009	6.9 ± 0.7	6.1 ± 0.5	6.6 ± 0.9	15.3 ± 1.2	19.2 ± 1.2	20.8 ± 2.3	169.8 ± 23.3	170.4 ± 23.4	173.5 ± 23.8
7.50	1.19 ± 0.007	1.21 ± 0.009	1.18 ± 0.009	5.1 ± 0.4	5.1 ± 0.5	4.6 ± 0.4	16.1 ± 1.1	19.6 ± 1.4	22.6 ± 1.5	165.1 ± 22.6	163.6 ± 22.4	166.5 ± 22.8
7.60	1.09 ± 0.007	1.10 ± 0.007	1.10 ± 0.006	4.4 ± 0.3	4.8 ± 0.4	4.5 ± 0.3	15.8 ± 1.1	19.4 ± 1.3	22.1 ± 1.4	174.8 ± 24.0	174.4 ± 23.9	174.4 ± 23.9
7.80	1.16 ± 0.007	1.16 ± 0.006	1.16 ± 0.006	6.5 ± 0.7	6.1 ± 0.5	5.0 ± 0.5	15.4 ± 1.4	18.6 ± 1.3	21.4 ± 2.0	167.7 ± 23.0	168.1 ± 23.1	167.9 ± 23.0
8.00	1.32 ± 0.01	1.32 ± 0.011	1.22 ± 0.009	6.0 ± 0.9	5.7 ± 0.7	13. ± 1.9	15.5 ± 2.0	18.7 ± 1.9	19.5 ± 3.0	153.8 ± 21.1	154.1 ± 21.1	162.3 ± 22.3
8.19	1.34 ± 0.005	1.33 ± 0.004	1.33 ± 0.005	7.2 ± 0.7	7.2 ± 0.5	6.2 ± 0.4	15.2 ± 1.2	18.7 ± 1.0	21.2 ± 1.2	152.7 ± 20.9	153.7 ± 21.1	153.6 ± 21.1
8.30	1.19 ± 0.008	1.19 ± 0.004	1.16 ± 0.005	5.1 ± 0.5	6.1 ± 0.4	6.6 ± 0.6	15.6 ± 1.2	19.0 ± 1.0	21.1 ± 1.7	164.9 ± 22.6	165.1 ± 22.6	168.0 ± 23.0
8.39	1.20 ± 0.006	1.20 ± 0.005	1.17 ± 0.005	6.5 ± 0.6	6.1 ± 0.5	8.5 ± 1.2	15.4 ± 1.2	18.8 ± 1.2	19.3 ± 2.2	164.0 ± 22.5	164.2 ± 22.5	166.8 ± 22.9
8.60	1.18 ± 0.007	1.20 ± 0.004	1.20 ± 0.005	7.6 ± 1.1	7.6 ± 0.7	6.9 ± 0.7	13.6 ± 1.5	18.5 ± 1.3	21.4 ± 1.7	166.3 ± 22.8	164.3 ± 22.5	164.5 ± 22.6
8.69	1.24 ± 0.006	1.24 ± 0.006	1.24 ± 0.005	6.3 ± 0.6	6.0 ± 0.5	5.6 ± 0.4	15.6 ± 1.1	19.1 ± 1.3	21.6 ± 1.4	160.9 ± 22.1	160.8 ± 22.1	160.6 ± 22.0
8.80	1.23 ± 0.009	1.23 ± 0.008	1.23 ± 0.008	8.7 ± 1.5	7.5 ± 1.0	7.3 ± 0.9	15.1 ± 2.1	18.4 ± 2.0	20.9 ± 2.2	161.7 ± 22.2	161.4 ± 22.1	161.6 ± 22.2

Continued on next page

Table 3 – continued from previous page

Time (MJD)	QPO Frequency (Hz)			Q-Value			RMS			Shock Location (X_s)		
	LE	ME	HE	LE	ME	HE	LE	ME	HE	LE	ME	HE
(1)	(2)	(3)	(4)	(5)	(6)	(7)	(8)	(9)	(10)	(11)	(12)	(13)
9.00	1.24 ± 0.008	1.23 ± 0.006	1.22 ± 0.009	7.3 ± 1.3	7.6 ± 0.3	10. ± 1.2	14.5 ± 2.0	19.6 ± 1.3	19.8 ± 1.3	160.8 ± 22.1	161.4 ± 22.1	162.2 ± 22.2
9.10	1.31 ± 0.005	1.30 ± 0.005	1.31 ± 0.005	6.8 ± 0.6	7.0 ± 0.5	6.6 ± 0.4	15.1 ± 1.1	18.5 ± 1.0	20.9 ± 1.1	155.1 ± 21.3	155.6 ± 21.3	155.1 ± 21.3
9.30	1.34 ± 0.006	1.34 ± 0.005	1.32 ± 0.007	6.2 ± 0.5	7.1 ± 0.7	7.3 ± 0.7	15.5 ± 1.1	18.6 ± 1.2	20.7 ± 1.6	152.8 ± 21.0	152.7 ± 20.9	153.8 ± 21.1
9.39	1.23 ± 0.008	1.25 ± 0.007	1.29 ± 0.007	4.5 ± 0.4	4.9 ± 0.3	6.5 ± 0.8	16.0 ± 1.3	19.6 ± 1.1	20.7 ± 2.1	161.2 ± 22.1	160.1 ± 22.0	156.6 ± 21.5
9.60	1.17 ± 0.005	1.17 ± 0.004	1.17 ± 0.004	7.6 ± 0.8	7.9 ± 0.8	6.5 ± 0.6	14.4 ± 1.2	17.7 ± 1.4	20.2 ± 1.5	167.1 ± 22.9	167.2 ± 22.9	167.0 ± 22.9
9.69	1.23 ± 0.01	1.23 ± 0.009	1.23 ± 0.009	4.0 ± 0.3	4.2 ± 0.3	4.1 ± 0.3	15.8 ± 1.0	18.6 ± 1.1	21.3 ± 1.2	161.3 ± 22.1	161.5 ± 22.2	161.6 ± 22.2
9.80	1.36 ± 0.01	1.33 ± 0.007	1.33 ± 0.009	5.5 ± 1.5	8.4 ± 0.4	5.9 ± 0.6	13.9 ± 2.7	18.5 ± 2.0	20.7 ± 1.9	151.4 ± 20.8	153.2 ± 21.0	153.2 ± 21.0
0.00	1.31 ± 0.01	1.32 ± 0.011	1.32 ± 0.011	7.0 ± 0.7	5.8 ± 1.2	11. ± 4.0	15.3 ± 2.1	18.5 ± 2.9	17.5 ± 4.4	154.7 ± 21.2	154.5 ± 21.2	154.0 ± 21.1
0.10	1.44 ± 0.01	1.44 ± 0.008	1.49 ± 0.008	5.3 ± 0.6	6.1 ± 0.5	7.1 ± 0.8	15.4 ± 1.3	18.6 ± 1.2	19.9 ± 1.6	145.6 ± 20.0	145.4 ± 19.9	142.1 ± 19.5
0.19	1.31 ± 0.005	1.32 ± 0.004	1.31 ± 0.003	6.6 ± 0.5	6.4 ± 0.4	6.3 ± 0.4	15.4 ± 1.0	18.6 ± 1.1	20.7 ± 1.1	154.9 ± 21.2	154.5 ± 21.2	154.6 ± 21.2
0.50	1.27 ± 0.006	1.27 ± 0.005	1.28 ± 0.005	7.2 ± 0.9	7.2 ± 0.7	8.4 ± 0.3	14.6 ± 1.5	18.1 ± 1.5	21.1 ± 1.0	158.5 ± 21.7	157.9 ± 21.7	157.6 ± 21.6
0.60	1.28 ± 0.007	1.30 ± 0.006	1.30 ± 0.006	7.3 ± 1.1	6.6 ± 0.5	6.0 ± 0.5	13.5 ± 1.4	18.1 ± 1.2	20.4 ± 1.4	157.1 ± 21.6	156.0 ± 21.4	155.9 ± 21.4
0.69	1.30 ± 0.007	1.30 ± 0.005	1.30 ± 0.005	6.6 ± 0.7	7.8 ± 0.8	7.0 ± 0.7	14.9 ± 1.3	17.8 ± 1.5	20.2 ± 1.7	156.1 ± 21.4	155.8 ± 21.4	155.7 ± 21.4
1.00	1.24 ± 0.008	1.23 ± 0.007	1.25 ± 0.011	6.5 ± 0.4	6.6 ± 0.7	7.1 ± 1.7	15.4 ± 1.2	18.5 ± 1.7	21.2 ± 3.9	161.1 ± 22.1	161.6 ± 22.2	159.5 ± 21.9
1.10	1.25 ± 0.007	1.25 ± 0.005	1.25 ± 0.005	5.0 ± 0.4	5.6 ± 0.3	5.4 ± 0.3	15.3 ± 1.0	18.6 ± 1.0	21.0 ± 1.1	159.8 ± 21.9	159.7 ± 21.9	159.7 ± 21.9
1.30	1.18 ± 0.009	1.17 ± 0.005	1.20 ± 0.004	6.0 ± 0.9	6.7 ± 0.5	7.5 ± 0.7	14.1 ± 1.5	17.6 ± 1.1	18.2 ± 1.4	166.0 ± 22.8	166.9 ± 22.9	163.9 ± 22.5
1.39	1.12 ± 0.008	1.13 ± 0.007	1.14 ± 0.009	4.7 ± 0.5	6.0 ± 0.5	4.9 ± 0.5	15.3 ± 1.2	18.0 ± 1.3	20.4 ± 1.9	171.9 ± 23.6	171.3 ± 23.5	170.0 ± 23.3
1.50	1.18 ± 0.006	1.17 ± 0.004	1.17 ± 0.004	5.8 ± 0.7	6.4 ± 0.6	6.6 ± 0.5	14.8 ± 1.4	17.5 ± 1.4	19.8 ± 1.4	166.5 ± 22.8	166.7 ± 22.9	167.1 ± 22.9
1.69	1.09 ± 0.007	1.08 ± 0.005	1.08 ± 0.005	4.6 ± 0.5	6.0 ± 0.5	6.0 ± 0.5	15.5 ± 1.4	17.9 ± 1.3	20.3 ± 1.4	175.5 ± 24.1	176.0 ± 24.1	175.8 ± 24.1
1.80	1.07 ± 0.01	1.08 ± 0.011	1.08 ± 0.009	5.9 ± 1.0	5.8 ± 1.0	5.4 ± 0.7	14.9 ± 2.0	17.1 ± 2.3	20.8 ± 2.5	177.5 ± 24.3	176.0 ± 24.1	175.9 ± 24.1
2.10	1.11 ± 0.008	1.12 ± 0.004	1.10 ± 0.005	6.0 ± 0.9	6.1 ± 0.4	6.5 ± 0.6	14.5 ± 1.6	17.7 ± 1.1	19.9 ± 1.4	172.7 ± 23.7	172.3 ± 23.6	174.2 ± 23.9
2.19	1.11 ± 0.007	1.10 ± 0.004	1.10 ± 0.004	5.9 ± 0.6	6.1 ± 0.5	6.0 ± 0.5	14.7 ± 1.2	17.6 ± 1.2	19.9 ± 1.2	173.4 ± 23.8	173.9 ± 23.9	173.7 ± 23.8
2.30	1.24 ± 0.01	1.25 ± 0.009	1.31 ± 0.011	4.1 ± 0.4	4.7 ± 0.3	7.0 ± 1.3	15.6 ± 1.2	17.8 ± 1.0	18.6 ± 2.9	161.0 ± 22.1	159.7 ± 21.9	155.1 ± 21.3
2.50	1.50 ± 0.01	1.49 ± 0.009	1.48 ± 0.009	4.5 ± 0.4	5.4 ± 0.4	5.5 ± 0.2	14.1 ± 1.0	17.7 ± 1.0	20.9 ± 0.8	141.9 ± 19.5	142.1 ± 19.5	143.0 ± 19.6
2.60	1.45 ± 0.009	1.46 ± 0.006	1.46 ± 0.006	5.5 ± 0.7	6.2 ± 0.5	6.0 ± 0.4	14.7 ± 1.4	18.0 ± 1.1	20.1 ± 1.2	144.8 ± 19.9	143.9 ± 19.7	143.9 ± 19.7
2.69	1.37 ± 0.007	1.38 ± 0.006	1.37 ± 0.007	8.0 ± 1.1	8.0 ± 0.8	7.2 ± 0.8	14.3 ± 1.4	17.3 ± 1.5	19.5 ± 1.6	150.4 ± 20.6	149.8 ± 20.5	150.1 ± 20.6
3.00	1.45 ± 0.01	1.46 ± 0.005	1.46 ± 0.009	7.7 ± 1.2	8.1 ± 0.8	8.0 ± 1.3	13.3 ± 1.5	17.2 ± 1.3	18.4 ± 2.4	145.0 ± 19.9	144.4 ± 19.8	144.1 ± 19.8
3.10	1.47 ± 0.009	1.47 ± 0.005	1.47 ± 0.004	6.4 ± 0.6	6.8 ± 0.4	6.6 ± 0.4	14.0 ± 1.0	17.5 ± 0.9	19.3 ± 1.0	143.6 ± 19.7	143.3 ± 19.6	143.5 ± 19.7
3.30	1.41 ± 0.008	1.40 ± 0.004	1.42 ± 0.006	5.3 ± 0.5	7.4 ± 0.5	7.6 ± 0.8	14.5 ± 1.2	17.4 ± 1.0	19.1 ± 1.6	147.3 ± 20.2	147.9 ± 20.3	146.7 ± 20.1
3.39	1.37 ± 0.01	1.35 ± 0.006	1.39 ± 0.008	5.5 ± 0.7	5.7 ± 0.4	5.6 ± 0.5	14.3 ± 1.3	17.7 ± 1.0	19.5 ± 1.3	150.6 ± 20.7	152.1 ± 20.9	149.3 ± 20.5
4.10	1.30 ± 0.01	1.28 ± 0.008	1.28 ± 0.009	3.5 ± 0.3	4.3 ± 0.2	3.7 ± 0.2	15.3 ± 1.1	17.4 ± 0.8	20.5 ± 0.9	155.6 ± 21.3	157.0 ± 21.5	157.1 ± 21.6
4.19	1.28 ± 0.01	1.28 ± 0.006	1.25 ± 0.006	5.7 ± 0.6	5.8 ± 0.5	7.2 ± 0.8	14.7 ± 1.3	17.5 ± 1.1	19.1 ± 1.6	157.4 ± 21.6	157.5 ± 21.6	160.1 ± 22.0
4.39	1.39 ± 0.01	1.39 ± 0.005	1.39 ± 0.006	5.3 ± 0.8	6.5 ± 0.5	6.3 ± 0.6	14.4 ± 1.4	17.4 ± 1.0	19.0 ± 1.3	148.6 ± 20.4	149.2 ± 20.5	148.7 ± 20.4
4.50	1.49 ± 0.01	1.49 ± 0.007	1.49 ± 0.007	5.0 ± 0.5	5.9 ± 0.4	5.6 ± 0.3	14.7 ± 1.1	17.6 ± 1.0	19.8 ± 1.1	142.0 ± 19.5	142.3 ± 19.5	142.5 ± 19.5
4.89	1.39 ± 0.01	1.40 ± 0.011	1.47 ± 0.033	8.7 ± 4.1	7.5 ± 1.5	7.5 ± 5.2	12.0 ± 4.3	16.3 ± 2.5	15.4 ± 6.8	149.0 ± 20.4	148.3 ± 20.3	143.6 ± 19.7
5.00	1.30 ± 0.006	1.30 ± 0.005	1.30 ± 0.005	6.1 ± 0.2	5.8 ± 0.4	5.4 ± 0.4	15.3 ± 0.7	17.0 ± 1.0	19.2 ± 1.2	155.8 ± 21.4	155.9 ± 21.4	155.9 ± 21.4
5.19	1.30 ± 0.01	1.31 ± 0.006	1.29 ± 0.006	5.0 ± 0.7	5.6 ± 0.4	5.6 ± 0.5	14.3 ± 1.3	17.3 ± 1.0	18.8 ± 1.3	155.4 ± 21.3	154.7 ± 21.2	156.3 ± 21.4
5.30	1.39 ± 0.009	1.38 ± 0.005	1.38 ± 0.007	5.9 ± 0.7	7.2 ± 0.6	6.8 ± 0.8	14.0 ± 1.3	16.5 ± 1.1	18.3 ± 1.7	149.2 ± 20.5	149.5 ± 20.5	149.9 ± 20.6
5.39	1.39 ± 0.01	1.39 ± 0.005	1.39 ± 0.004	6.0 ± 0.8	6.6 ± 0.5	5.8 ± 0.4	13.6 ± 1.3	16.7 ± 1.0	21.5 ± 1.0	149.2 ± 20.5	148.7 ± 20.4	148.7 ± 20.4
5.60	1.29 ± 0.009	1.31 ± 0.006	1.32 ± 0.006	6.9 ± 0.9	6.2 ± 0.5	5.6 ± 0.4	13.5 ± 1.3	17.0 ± 1.1	19.5 ± 1.1	156.4 ± 21.5	155.2 ± 21.3	154.5 ± 21.2
5.69	1.37 ± 0.01	1.37 ± 0.008	1.35 ± 0.008	6.2 ± 1.6	7.6 ± 1.0	6.1 ± 0.8	13.4 ± 2.6	15.8 ± 1.7	17.6 ± 1.9	150.7 ± 20.7	150.6 ± 20.6	151.6 ± 20.8
6.00	1.39 ± 0.01	1.40 ± 0.006	1.39 ± 0.006	5.3 ± 0.8	5.9 ± 0.4	5.6 ± 0.4	13.8 ± 1.5	16.9 ± 0.9	18.8 ± 1.0	148.8 ± 20.4	148.2 ± 20.3	148.9 ± 20.4

Continued on next page

Table 3 – continued from previous page

Time	QPO Frequency (Hz)			Q-Value			RMS			Shock Location (X_s)		
(MJD)	LE	ME	HE	LE	ME	HE	LE	ME	HE	LE	ME	HE
(1)	(2)	(3)	(4)	(5)	(6)	(7)	(8)	(9)	(10)	(11)	(12)	(13)
6.19	1.37 ± 0.008	1.38 ± 0.004	1.39 ± 0.006	7.5 ± 1.2	7.3 ± 0.6	7.5 ± 0.8	13.2 ± 1.5	16.4 ± 1.1	17.9 ± 1.5	150.5 ± 20.6	149.6 ± 20.5	149.3 ± 20.5
6.30	1.24 ± 0.01	1.26 ± 0.006	1.25 ± 0.009	6.1 ± 0.9	6.8 ± 0.7	6.6 ± 1.0	13.8 ± 1.5	16.2 ± 1.2	18.3 ± 2.0	160.6 ± 22.0	158.6 ± 21.8	160.0 ± 21.9
6.39	1.23 ± 0.01	1.24 ± 0.007	1.24 ± 0.006	5.0 ± 0.8	5.2 ± 0.4	4.8 ± 0.3	14.0 ± 1.5	17.0 ± 1.0	19.4 ± 1.2	161.7 ± 22.2	160.4 ± 22.0	161.0 ± 22.1
6.60	1.11 ± 0.008	1.12 ± 0.005	1.12 ± 0.004	7.6 ± 1.3	6.7 ± 0.6	5.7 ± 0.5	13.8 ± 1.9	20.4 ± 1.2	18.8 ± 1.3	172.6 ± 23.7	171.9 ± 23.6	172.1 ± 23.6
7.00	1.29 ± 0.008	1.25 ± 0.006	1.30 ± 0.005	5.6 ± 0.2	8.2 ± 0.2	5.6 ± 0.4	15.2 ± 0.8	17.4 ± 3.7	18.7 ± 1.1	156.3 ± 21.4	159.4 ± 21.9	155.4 ± 21.3
7.10	1.45 ± 0.008	1.45 ± 0.005	1.45 ± 0.005	7.0 ± 0.9	7.9 ± 0.7	9.3 ± 0.5	13.1 ± 1.3	15.8 ± 1.2	18.4 ± 1.8	144.9 ± 19.9	144.7 ± 19.8	144.8 ± 19.9
7.30	1.50 ± 0.008	1.51 ± 0.005	1.51 ± 0.007	5.8 ± 0.7	7.3 ± 0.5	7.0 ± 0.6	13.3 ± 1.3	16.7 ± 1.0	18.3 ± 1.4	141.7 ± 19.4	141.2 ± 19.4	140.9 ± 19.3
7.39	1.42 ± 0.009	1.43 ± 0.004	1.42 ± 0.005	6.9 ± 1.1	6.6 ± 0.4	5.8 ± 0.4	13.2 ± 1.4	16.4 ± 1.0	18.4 ± 1.0	146.8 ± 20.1	146.5 ± 20.1	146.8 ± 20.1
7.60	1.45 ± 0.009	1.43 ± 0.005	1.43 ± 0.005	6.4 ± 1.1	6.8 ± 0.5	6.7 ± 0.5	12.9 ± 1.6	16.0 ± 1.0	17.3 ± 1.1	144.6 ± 19.8	146.3 ± 20.1	145.9 ± 20.0
7.80	1.69 ± 0.02	1.79 ± 0.011	1.78 ± 0.011	5.6 ± 1.8	4.0 ± 0.4	8.3 ± 2.4	13.1 ± 3.2	17.3 ± 1.5	15.0 ± 3.1	130.7 ± 17.9	125.7 ± 17.2	126.3 ± 17.3
8.00	1.85 ± 0.01	1.84 ± 0.004	1.84 ± 0.005	6.9 ± 0.8	6.9 ± 0.3	6.6 ± 0.3	12.5 ± 1.2	16.6 ± 0.7	18.3 ± 0.8	123.0 ± 16.9	123.7 ± 17.0	123.4 ± 16.9

In column 1, we have listed the MJD-60180 (to save space) of the exposure IDs we used.
Columns 2, 3, & 4 represent the QPO frequency in LE, ME, and HE energy bands respectively.
Columns 5, 6, & 7 represent the Q-values of QPOs in LE, ME, and HE energy bands respectively.
Columns 8, 9, & 10 represent the QPO RMS (%) in LE, ME, and HE energy bands respectively.
Columns 11, 12, & 13 represent the shock location in LE, ME, and HE energy bands respectively.

Table 4. Properties from spectral analysis

Time MJD (Day)	TBabs N_H (cm^{-2})	gabs			diskbb		power-law		Gaussian			pexrav					χ^2/DOF
(1)	(2)	E_{abs} (keV)	σ_{abs} (keV)	N_{abs} (keV)	T_{in} (keV)	Norm	Γ	Norm	E_g (keV)	σ_g (keV)	Norm ($\text{ph}/\text{cm}^2/\text{s}$)	Γ	E_{cut} (keV)	R_{ref}	cos(i) ($^\circ$)	Norm	χ^2/DOF
(1)	(2)	(3)	(4)	(5)	(6)	(7)	(8)	(9)	(10)	(11)	(12)	(13)	(14)	(15)	(16)	(17)	(18)
60181.4	0.1859 ± 3.1E-3	1.780 ± 3.2E-2	0.4000 ± 2.2E-2	0.1797 ± 7.5E-3	0.1797 ± 2.2E-3	1.8E+05 ± 1.6E+3	2.1238 ± 9.4E-3	13.084 ± 0.969	5.252 ± 5.4E-2	-21.920 ± 6.9E-2	0.8232 ± 3.5E-2	1.1406 ± 7.1E-2	26.25 ± 0.98	0.4000 ± 4.5E-3	0.4912 ± 6.2E-3	3.32 ± 0.37	1384.50/1401
60181.6	0.1859 ± 6.8E-3	1.798 ± 6.1E-2	0.2289 ± 3.6E-2	1.1E-2 ± 1.4E-3	0.1999 ± 1.1E-2	1.9E+05 ± 1.1E+3	2.1612 ± 1.9E-2	18.201 ± 1.925	5.482 ± 5.1E-2	-21.621 ± 6.1E-2	0.6342 ± 2.9E-2	0.9422 ± 8.4E-2	20.33 ± 1.15	0.5000 ± 5.0E-2	0.1944 ± 1.6E-2	2.70 ± 0.70	1375.43/1401
60181.7	0.1859 ± 5.3E-3	1.650 ± 4.8E-2	4.0E-2 ± 2.8E-2	1.0E-2 ± 1.1E-3	0.2989 ± 1.7E-2	1.1E+05 ± 2.6E+3	2.1053 ± 1.8E-2	15.134 ± 1.748	5.621 ± 4.5E-2	-20.917 ± 5.6E-2	0.2047 ± 2.3E-2	1.0043 ± 6.1E-2	20.07 ± 0.86	0.4986 ± 8.2E-4	5.1E-2 ± 2.1E-2	4.45 ± 0.68	1341.34/1283
60182.1	0.1859 ± 9.0E-3	1.650 ± 3.0E-2	4.0E-2 ± 2.7E-2	1.0E-2 ± 6.9E-3	0.2650 ± 1.8E-4	1.1E+05 ± 3.8E+3	2.1553 ± 9.5E-2	18.462 ± 4.4E-2	5.552 ± 8.5E-2	0.877 ± 0.1067	0.2584 ± 5.6E-2	1.0053 ± 0.1639	17.84 ± 2.30	0.4740 ± 8.6E-2	6.1E-2 ± 1.0E-2	5.26 ± 1.8E-2	1235.38/1283
60182.9	0.3859 ± 1.4E-2	1.950 ± 0.1323	0.3656 ± 2.1E-3	3.1E-2 ± 1.9E-3	0.3949 ± 1.9E-4	1.1E+05 ± 3.8E+3	1.9556 ± 1.6E-3	36.0786 ± 3.9E-2	5.417 ± 5.1E-2	-20.989 ± 6.8E-2	0.3876 ± 6.3E-2	1.3568 ± 0.2559	20.18 ± 3.47	0.4990 ± 8.1E-5	8.0E-2 ± 2.1E-3	317.2 ± 1.5E-2	1220.62/1283
60183.1	0.3859 ± 4.7E-2	1.901 ± 1.6E-2	0.4000 ± 2.3E-2	5.7E-2 ± 1.9E-3	0.3353 ± 3.5E-3	7.8E+6 ± 3.6E+4	1.9805 ± 2.5E-2	6.2591 ± 3.4086	5.288 ± 5.8E-2	-21.255 ± 6.4E-2	0.2621 ± 5.9E-2	1.3521 ± 6.9E-2	20.64 ± 0.71	5.7E-2 ± 4.7E-2	35.0E-2 ± 5.3E-3	317.4 ± 1.1E-2	1004.79/1313
60183.8	0.3859 ± 8.3E-3	1.764 ± 6.5E-3	0.3621 ± 8.7E-3	0.1800 ± 2.6E-3	0.2855 ± 2.6E-4	2.3E+06 ± 1.9E+4	1.9641 ± 3.2E-3	35.1858 ± 4.6E-2	5.478 ± 9.9E-2	-21.053 ± 8.4E-2	0.24529 ± 8.8E-2	1.4714 ± 8.9E-2	22.18 ± 1.71	1.0E-2 ± 6.7E-2	35.0E-2 ± 3.6E-2	323.9 ± 1.8E-2	1149.55/1313
60184.6	0.3500 ± 8.2E-3	1.768 ± 6.1E-3	0.3537 ± 8.3E-3	0.1799 ± 6.7E-3	0.2793 ± 2.5E-4	4.2E+06 ± 2.4E+4	1.9883 ± 1.9E-3	35.6874 ± 2.9E-2	5.446 ± 9.5E-2	-21.056 ± 8.0E-2	0.25005 ± 9.5E-2	1.5152 ± 9.0E-2	22.08 ± 1.77	1.0E-2 ± 6.9E-2	35.0E-2 ± 3.7E-2	327.1 ± 1.9E-2	1201.52/1303
60185.4	0.3500 ± 7.5E-3	1.799 ± 5.8E-3	0.3689 ± 7.7E-3	0.1800 ± 5.7E-3	0.2984 ± 2.2E-4	2.0E+06 ± 1.3E+4	2.0041 ± 1.9E-3	36.3291 ± 2.9E-2	5.342 ± 8.8E-2	-20.934 ± 8.3E-2	0.24323 ± 9.5E-2	1.5314 ± 9.8E-2	21.63 ± 1.87	1.0E-2 ± 6.4E-2	35.0E-2 ± 3.6E-2	328.2 ± 1.8E-2	1111.05/1285
60186.2	0.3500 ± 8.4E-3	1.756 ± 6.9E-3	0.3762 ± 6.9E-3	0.1800 ± 8.9E-3	0.3189 ± 2.8E-4	1.2E+06 ± 8918.9	2.1058 ± 1.7E-3	39.6845 ± 3.6E-2	5.305 ± 3.6E-2	-21.015 ± 0.1152	0.25269 ± 9.5E-2	1.5823 ± 0.1425	22.04 ± 2.65	1.0E-2 ± 6.9E-2	35.0E-2 ± 1.9E-3	329.0 ± 2.2E-2	1122.93/1285
60187.1	0.3276 ± 5.6E-3	1.950 ± 2.2E-2	0.4000 ± 2.9E-2	0.1306 ± 4.2E-3	0.3227 ± 3.6E-4	1.2E+06 ± 1.2E+4	2.0974 ± 2.5E-3	39.5144 ± 4.2E-2	5.354 ± 0.1790	0.948 ± 0.1523	0.4538 ± 6.6E-3	1.5803 ± 0.2594	21.77 ± 4.83	1.3E-2 ± 4.2E-2	35.1E-2 ± 9.1E-2	428.6 ± 2.4E-2	996.48/1285
60187.2	0.3500 ± 7.8E-3	1.799 ± 6.4E-3	0.3917 ± 8.6E-3	0.1800 ± 6.1E-3	0.3273 ± 2.5E-4	1.0E+06 ± 6693.9	2.1326 ± 1.5E-3	10.804 ± 3.5E-2	5.296 ± 0.1264	0.977 ± 0.1035	0.4905 ± 0.1346	1.6026 ± 0.1668	22.55 ± 3.18	1.0E-2 ± 6.6E-2	35.0E-2 ± 3.5E-2	428.7 ± 2.1E-2	1078.22/1285
60188.0	0.3166 ± 4.8E-3	1.815 ± 1.3E-2	0.4000 ± 3.3E-2	0.1113 ± 3.4E-3	0.3618 ± 4.1E-4	4.1E+06 ± 3606.1	2.1735 ± 2.3E-3	33.529 ± 5.5E-2	5.309 ± 0.1971	0.904 ± 2.7E-2	0.23923 ± 9.6E-3	1.6310 ± 0.3514	20.97 ± 3.10	0.5000 ± 7.7E-2	2.8E-2 ± 9.6E-2	327.8 ± 3.0E-2	1057.80/1313
60189.0	0.1203 ± 7.1E-3	1.950 ± 3.4E-2	0.2443 ± 1.9E-2	3.9E-2 ± 2.1E-2	0.3598 ± 6.3E-4	2.4E+05 ± 3216.2	2.1753 ± 2.3E-3	33.528 ± 4.9E-2	5.437 ± 0.1067	1.000 ± 2.5E-2	0.24316 ± 4.2E-2	1.6133 ± 0.3538	22.06 ± 6.38	0.5000 ± 1.1E-2	5.2E-2 ± 5.8E-2	327.8 ± 2.7E-2	1016.91/1313
60189.1	0.1200 ± 7.6E-3	1.712 ± 1.1E-2	0.3999 ± 2.9E-2	0.1136 ± 3.5E-3	0.3412 ± 4.6E-4	3.8E+05 ± 4145.9	2.1434 ± 1.6E-3	33.099 ± 3.5E-2	5.513 ± 1.7E-2	-21.000 ± 2.9E-2	0.24408 ± 5.3E-3	1.6954 ± 4.5E-2	24.35 ± 7E-2	2.1E-2 ± 6.6E-2	35.0E-2 ± 3.7E-2	332.1 ± 2.2E-2	1466.04/1431
60190.1	0.1200 ± 8.3E-3	1.950 ± 2.6E-2	0.2363 ± 1.4E-2	4.4E-2 ± 1.9E-3	0.3375 ± 5.6E-4	3.7E+05 ± 4960.2	2.1789 ± 1.9E-3	31.929 ± 4.3E-2	5.542 ± 2.4E-2	-21.000 ± 4.0E-2	0.23701 ± 6.2E-3	1.7417 ± 5.5E-4	24.79 ± 0.10	0.1711 ± 2.4E-2	0.1000 ± 4.1E-2	33.2 ± 2.7E-2	1271.40/1431
60191.0	0.2632 ± 4.6E-3	1.950 ± 3.9E-2	0.2229 ± 2.2E-2	3.0E-2 ± 4.2E-3	0.3650 ± 4.9E-4	2.7E+05 ± 2821.2	2.0287 ± 3.1E-3	36.6459 ± 3.8E-2	5.473 ± 3.3E-2	-20.899 ± 2.7E-2	0.22641 ± 6.6E-3	1.6578 ± 5.8E-4	23.46 ± 0.11	0.2205 ± 2.8E-2	9.8E-2 ± 1.8E-2	30.6 ± 2.6E-2	1124.73/1431
60191.1	0.3086 ± 0.0030	-	-	-	0.4137 ± 0.0017	9.8E+04 ± 1587.2	2.1029 ± 0.0085	8.423 ± 0.8943	5.509 ± 0.0500	1.000 ± 0.0645	0.3533 ± 0.030	1.6820 ± 0.0619	25.08 ± 0.87	1.0E-2 ± 0.004	5.0E-2 ± 0.0057	30.3 ± 0.328	1250.10/1434
60192.2	0.3376 ± 0.0067	-	-	-	0.4183 ± 0.0085	9.2E+04 ± 1091.2	2.0389 ± 0.0173	6.182 ± 1.7767	5.515 ± 0.0472	1.000 ± 0.0570	0.3479 ± 0.025	1.6420 ± 0.0732	25.44 ± 1.03	1.0E-2 ± 0.045	5.0E-2 ± 0.0048	27.7 ± 0.621	1232.74/1434
60193.4	0.2517 ± 0.0052	-	-	-	0.4298 ± 0.0131	6.4E+04 ± 2579.2	2.2491 ± 0.0164	16.79 ± 1.6134	5.471 ± 0.0416	1.000 ± 0.0523	0.4039 ± 0.020	1.6530 ± 0.0531	24.97 ± 0.77	1.1E-2 ± 0.000	0.1000 ± 0.0094	23.7 ± 0.603	1496.21/1434
60194.1	0.3500 ± 0.0055	-	-	-	0.4204 ± 0.0035	1.0E+05 ± 4960.0	2.0766 ± 0.0192	7.510 ± 1.8635	5.460 ± 0.0407	0.689 ± 0.0495	0.1901 ± 0.021	1.6560 ± 0.0540	25.60 ± 0.77	1.0E-2 ± 0.009	5.0E-2 ± 0.003	26.9 ± 0.0661	1177.08/1434
60194.5	0.1200 ± 0.0023	-	-	-	0.4526 ± 0.0001	2.5E+04 ± 2083.2	2.2001 ± 0.0944	10.89 ± 0.3239	5.572 ± 0.0951	1.000 ± 0.1342	0.4107 ± 0.066	1.8360 ± 0.1095	29.50 ± 1.89	0.52 ± 0.008	0.10 ± 0.005	32.0 ± 0.0241	1697.08/1428
60195.0	0.3500 ± 0.0089	-	-	-	0.4204 ± 0.0001	9.8E+04 ± 3273.6	2.0180 ± 0.0866	5.491 ± 0.0406	5.525 ± 0.0787	0.713 ± 0.0997	0.1504 ± 0.049	1.6800 ± 0.1429	26.42 ± 2.06	1.0E-2 ± 0.007	5.0E-2 ± 0.008	27.9 ± 0.0092	1048.98/1432
60195.2	0.3500 ± 0.0088	-	-	-	0.4240 ± 0.0002	9.1E+04 ± 6844.8	2.0143 ± 0.0024	5.500 ± 0.0609	5.504 ± 0.0407	0.728 ± 0.0504	0.1716 ± 0.035	1.6820 ± 0.1555	26.52 ± 1.88	1.0E-2 ± 0.072	5.0E-2 ± 0.0030	27.9 ± 0.007	1070.82/1432
60195.6	0.1202 ± 0.0468	-	-	-	0.3834 ± 0.0027	5.7E+04 ± 3571.2	2.1645 ± 0.0228	8.874 ± 1.1461	5.593 ± 0.0537	1.000 ± 0.0598	0.4149 ± 0.051	1.8000 ± 0.0601	30.54 ± 0.63	0.42 ± 0.004	9.9E-2 ± 0.0049	29.0 ± 0.009	1515.80/1430
60196.0	0.3500 ± 0.0082	-	-	-	0.4296 ± 0.0002	8.4E+04 ± 1884.8	2.0542 ± 0.0029	6.241 ± 0.0424	5.515 ± 0.0916	0.736 ± 0.0785	0.1505 ± 0.077	1.7180 ± 0.0776	27.78 ± 1.53	1.0E-2 ± 0.006	5.0E-2 ± 0.0033	28.6 ± 0.015	1048.18/1434
60196.2	0.3500 ± 0.0081	-	-	-	0.4315 ± 0.0001	8.4E+04 ± 2380.8	2.0562 ± 0.0017	6.572 ± 0.0267	5.548 ± 0.0879	0.657 ± 0.0748	0.1340 ± 0.083	1.6910 ± 0.0784	26.73 ± 1.58	6.4E-2 ± 0.006	5.0E-2 ± 0.0034	27.3 ± 0.016	1036.34/1434
60196.6	0.1201 ± 0.0074	-	-	-	0.3545 ± 0.0001	1.0E+05 ± 1289.6	2.0491 ± 0.0017	5.511 ± 0.0267	5.607 ± 0.0814	1.000 ± 0.0776	0.3877 ± 0.083	1.7610 ± 0.0854	29.76 ± 1.67	0.44 ± 0.005	9.9E-2 ± 0.0033	27.6 ± 0.015	1517.31/1434
60197.0	0.3453 ± 0.0083	-	-	-	0.4326 ± 0.0002	7.7E+04 ± 8846.9	1.9867 ± 0.0015	4.390 ± 0.0332	5.569 ± 0.0333	0.707 ± 0.1077	0.1417 ± 0.083	1.6960 ± 0.1242	28.60 ± 2.37	0.14 ± 0.006	5.0E-2 ± 0.0017	27.0 ± 0.019	1009.58/1434
60197.1	0.3500 ± 0.0055	-	-	-	0.4333 ± 0.0002	7.9E+04 ± 1190.4	2.0631 ± 0.0002	6.810 ± 0.0387	5.441 ± 0.1657	0.749 ± 0.1424	0.1654 ± 0.005	1.7280 ± 0.2261	27.24 ± 4.33	0.31 ± 0.003	5.0E-2 ± 0.0008	27.5 ± 0.021	1108.23/1434
60197.6	0.1200 ± 0.0077	-	-	-	0.4298 ± 0.0001	2.8E+04 ± 6640.3	2.2020 ± 0.0013	10.47 ± 0.0323	5.614 ± 0.1170	1.000 ± 0.0967	0.3532 ± 0.017	1.8330 ± 0.1454	31.74 ± 2.85	0.50 ± 0.006	0.10 ± 0.0003	28.2 ± 0.018	1455.99/1434
60198.0	0.3500 ± 0.0047	-	-	-	0.4176 ± 0.0003	9.1E+04 ± 3577.2	2.1415 ± 0.0020	8.122 ± 0.0507	5.519 ± 0.1825	0.548 ± 0.0252	0.1061 ± 0.008	1.8990 ± 0.3064	31.93 ± 2.78	0.50 ± 0.007	8.7E-2 ± 0.0089	35.7 ± 0.026	1087.43/1434

Column 1 represents the MJD of those respective Exposure IDs for which we have performed spectral analysis.

Column 2 gives the values of hydrogen column densities (N_H) of those analyzed exposures.

Columns 3, 4, & 5 give the values of the parameters of the ‘gabs’ model.

Columns 6 & 7 give the model fitted values of the parameters from the ‘diskbb’ model.

Columns 8 & 9 give the model fitted values of the parameters from the ‘power-law’ model.

Columns 10, 11, & 12 give the model fitted values of the parameters from the ‘Gaussian’ model.

Columns 13–17 give the model fitted values of the parameters from the ‘pexrav’ model.

Column 18 gives χ^2/DOF values of the respective spectral fits.

